

1 **Dislocation creep of olivine: Backstress evolution** 2 **controls transient creep at high temperatures**

3 Lars N. Hansen^{1*}, David Wallis^{2†}, Thomas Breithaupt³, Christopher A. Thom³, Imogen Kempton³

4 ¹Department of Earth and Environmental Sciences, University of Minnesota, Minneapolis, 55455, United
5 States of America

6 ²Department of Earth Sciences, Utrecht University, Utrecht, 3584 CB, The Netherlands

7 ³Department of Earth Sciences, University of Oxford, Oxford, OX1 3AN, United Kingdom

8 [†]Present address: Department of Earth Sciences, University of Cambridge, Cambridge, CB2 3EQ, United
9 Kingdom

10 *corresponding author: lnhansen@umn.edu

11 Keywords: olivine, dislocation creep, transient creep, backstress, dislocation interactions, stress-reduction
12 tests, mantle viscosity

13 **Abstract**

14 Transient creep occurs during geodynamic processes that impose stress changes on rocks at high
15 temperatures. The transient is manifested as evolution in the viscosity of the rocks until steady-state flow
16 is achieved. Although several phenomenological models of transient creep in rocks have been proposed,
17 the dominant microphysical processes that control such behavior remain poorly constrained. To identify
18 the intragranular processes that contribute to transient creep of olivine, we performed stress-reduction

19 tests on single crystals of olivine at temperatures of 1250–1300°C. In these experiments, samples undergo
20 time-dependent reverse strain after the stress reduction. The magnitude of reverse strain is $\sim 10^{-3}$ and
21 increases with increasing magnitude of the stress reduction. High-angular resolution electron backscatter
22 diffraction analyses of deformed material reveal lattice curvature and heterogeneous stresses associated
23 with the dominant slip system. The mechanical and microstructural data are consistent with transient
24 creep of the single crystals arising from accumulation and release of backstresses among dislocations.
25 These results allow the dislocation-glide component of creep at high temperatures to be isolated, and we
26 use these data to calibrate a flow law for olivine to describe the glide component of creep over a wide
27 temperature range. We argue that this flow law can be used to estimate both transient creep and steady-
28 state viscosities of olivine, with the transient evolution controlled by the evolution of the backstress. This
29 model is able to predict variability in the style of transient (normal versus inverse) and the load-relaxation
30 response observed in previous work.

31 **1 Introduction**

32 The evolution of viscosity during flow of mantle rocks at high temperatures is fundamental to a variety of
33 geodynamic processes. For example, transient creep of the upper mantle has been identified as a major
34 contributor to geodetically observed surface deformations during post-seismic creep (Pollitz 2005; Freed,
35 Hirth, and Behn 2012; Masuti et al. 2016; Qiu et al. 2018), for which the strains are typically $< 10^{-3}$, and
36 inferred viscosities are one to two orders of magnitude lower than the long-term, steady-state viscosity.
37 Because transient viscosities also continue to evolve during postseismic deformation, they likely cause a
38 time-dependent transfer of stresses to neighbouring faults, rather than the instantaneous transfer assumed
39 by popular calculations of Coloumb stress changes (e.g., Freed 2005). Although sophisticated earthquake
40 forecast models do incorporate time-dependent loading according to average plate motion rates (e.g.,
41 Field et al. 2015, 2017), they still do not incorporate variable loading rates that would occur due to

42 transient creep of the lithosphere. In addition, transient viscosities are expected to be important, although
43 they have not yet been thoroughly considered, in other small-strain processes including flexure of the
44 lithosphere near volcanic loads (Zhong and Watts 2013) or in subducting slabs near trenches (Hunter and
45 Watts 2016), during which the strains rarely exceed 10^{-2} .

46 Although by far the bulk of investigations into the rheological behavior of the upper mantle have focused
47 on measuring and predicting steady-state viscosities in olivine attained under constant applied stress (e.g.,
48 Hirth and Kohlstedt 2003), some experiments have been conducted to investigate transient creep in
49 olivine. These experimental data confirm that the initial viscosities at the onset of creep or just after other
50 abrupt changes in stress are typically several orders of magnitude lower than the eventual steady-state
51 viscosities (Post 1977; Smith and Carpenter 1987; Hanson and Spetzler 1994; Chopra 1997). These rapid
52 changes in viscosity occur over the initial strain increments of $<10^{-2}$, and the most likely microstructural
53 changes responsible for this evolution are changes in the distribution and arrangement of dislocations
54 (Hanson and Spetzler 1994; S. Karato and Spetzler 1990; Durham, Goetze, and Blake 1977). However,
55 there are certain cases in which the initial viscosity is higher at the onset of creep and decreases with
56 progressive deformation, which is referred to as an “inverse” transient. Hanson and Spetzler (1994)
57 observed that single crystals of olivine can exhibit either a normal or an inverse transient, depending on
58 the orientation of loading. In addition, Cooper et al. (2016) observed that the type of transient can change
59 in a single experiment as the applied stress is gradually increased. This variability in observations
60 highlights that the specifics of the microstructural evolution and its link to both transient creep and
61 steady-state creep remain poorly constrained.

62 Due to the complexity of, and uncertainty regarding, potential micromechanical processes involved,
63 experimental observations of transient creep have generally been fit by empirical models in which the
64 underlying physics is not investigated. The Burgers model is often employed (Smith and Carpenter 1987;

65 Chopra 1997), amongst several others (Post 1977; Hanson and Spetzler 1994). However, the lack of a
66 rigorous microphysical basis to these models limits confidence in extrapolating them to predict
67 deformation at natural conditions under which the key processes potentially differ from those in
68 experiments. Moreover, as these processes and associated microstructural changes are poorly constrained,
69 model predictions cannot easily be tested against the microstructures of natural rocks. Thus, there remains
70 a need to establish the fundamental microphysics of transient creep.

71 Distinguishing among different models of transient creep is difficult. In general, the experimentalist is
72 tasked with fitting models to strain-time curves or strain rate-time curves, for which differences among
73 models are subtle (Post 1977; Hanson and Spetzler 1994). Additional constraints can potentially be
74 gleaned from the microstructures of deformed materials (Hanson and Spetzler 1994). However, the small
75 strains involved can result in microstructural changes beyond the resolution of some common
76 observational techniques, such as standard electron backscatter diffraction (EBSD) (Thieme et al. 2018).

77 We alleviate these problems by using stress-reduction experiments. These tests involve applying a rapid
78 reduction in stress to a sample undergoing steady-state creep and have been applied extensively to the
79 study of engineering materials (Blum and Weckert 1987; Biberger and Gibeling 1995; Poirier 1977).
80 Stress reductions typically induce an ensuing period of transient creep. As each test requires only a small
81 strain interval and causes only limited modification of the microstructure, multiple tests can be performed
82 on a sample within one experiment (e.g., with different magnitudes of stress reduction). Unlike increases
83 in stress magnitude, which are always followed by ongoing creep in the original direction, reductions in
84 stress can also result in a period of anelastic reverse strain (Blum and Weckert 1987; Biberger and
85 Gibeling 1995; Poirier 1977). As such, stress-reduction tests provide a wide variety of characteristics
86 against which to test models of transient creep.

87 Despite their potential, stress-reduction tests have been underutilized for geological minerals. Stress-
88 reduction tests have been applied to ice (Meyssonnier and Goubert 1994; Caswell, Cooper, and Goldsby
89 2015) and garnet (Z. Wang, Karato, and Fujino 1996). Applications to olivine have been limited primarily
90 to torsional microcreep experiments on fine-grained aggregates by Gribb and Cooper (1998) and Jackson
91 et al. (2002; 2014). Chopra (1997) reported two experiments on natural dunites, and Cooper et al. (2016)
92 reported one experiment on a single crystal. However, the microphysical controls on the behaviour
93 exhibited in such tests have not been systematically investigated.

94 Here we report stress-reduction experiments on single crystals of olivine to isolate and investigate
95 transient creep arising from intragranular processes. We analyse the microstructures of the deformed
96 samples using high-angular resolution electron backscatter diffraction (HR-EBSD) (Wilkinson, Meaden,
97 and Dingley 2006; D. Wallis et al. 2019), which is ideally suited to detecting subtle microstructural
98 changes, including lattice rotations and stress heterogeneities associated with geometrically necessary
99 dislocations (GNDs). We combine the results with previous rheological data to constrain the
100 microphysical processes that control the transient viscosity of rocks after rapid stress changes and make
101 predictions about the variability in rheological behavior that may be observed during transient creep in
102 Earth.

103 **2 Methods**

104 ***2.1 Sample preparation***

105 Four samples were prepared from gem-quality single crystals of San Carlos olivine. Rough crystals were
106 oriented using EBSD. The crystals were cut into rectangular parallelepipeds, with lengths in the range of
107 2 to 5 mm and aspect ratios in the range of 2:1 to 3:1, that were free from visible cracks and inclusions.
108 Samples were cut with long axes corresponding to the $[110]_c$, $[101]_c$, and $[011]_c$ orientations, following
109 the notation of Durham and Goetze (1977), with the intention of maximizing the resolved shear stress on

110 the (010)[100], (001)[100] and (100)[001], and (010)[001] slip systems, respectively. The end faces of
111 samples were ground flat and parallel using 1500 grit SiC paper.

112 ***2.2 Deformation experiments***

113 Deformation experiments were conducted in a 1-atm uniaxial creep apparatus in the Rock Rheology
114 Laboratory at the University of Oxford. Details of the apparatus design are provided by Cao et al. (2020).
115 Samples were placed in direct contact with alumina platens, which were in direct contact with SiC
116 pistons. Although San Carlos olivine and alumina are not in chemical equilibrium, reaction products were
117 not visible after experiments, indicating that any reaction was limited in extent. The loading column is
118 housed inside a vertical tube furnace. The hot zone of the furnace is >5 cm, and temperature was
119 controlled with a thermocouple placed within 1 cm of the sample. The temperature difference across the
120 samples was <1°C. The oxygen fugacity was controlled with a mixture of CO and CO₂, and the ratio of
121 gas flow rates was maintained constant to set the oxygen fugacity at a value of 10⁻⁸ to 10^{-7.5} atm, near the
122 Ni:NiO buffer at the temperatures of the experiments. A gas-tight seal was maintained on the moving SiC
123 piston by means of frictionless oil bellows. An axial load was applied to the loading column with a
124 piezoelectric actuator using a closed-loop servo-control system, and the load was measured and controlled
125 with a precision of ~1 N. Changes in sample length were assessed by measuring displacements of the SiC
126 piston relative to the loading frame. Displacements were measured with a linear encoder with resolution
127 of 10 nm and corrected for distortion of the apparatus using the complex compliance of the apparatus
128 calibrated by Cao et al. (2020).

129 Samples were initially subjected to a small compressive load (~10 N) using the piezoelectric actuator to
130 ensure that contact was maintained with pistons and the sample remained upright and aligned throughout
131 the heating procedure. Samples were heated to temperatures of either 1250 or 1300°C over the course of

132 approximately 3 hours. Deformation was not initiated until the measured temperature reached and
 133 maintained a steady value within 1°C of the set point.

134 Once the temperature stabilized, the load was gradually increased at a constant rate to the desired value,
 135 corresponding to stresses of 77 to 189 MPa, over the course of ~120 s. An example of the stress and strain
 136 evolution for experiment OxR0009 is illustrated in Figure 1. The load was maintained at the desired
 137 value, and the displacement was monitored until an approximately steady-state displacement rate was
 138 achieved, which typically required 2 to 5% strain. At this point, the load was reduced to a new set point at
 139 the maximum rate achievable by the apparatus, which was on the order of ~10 ms for the largest stress
 140 reductions. In order to record this deformation with sufficient resolution, the data sampling rate was
 141 increased from 0.1 Hz to 100 kHz just prior to the load reduction and then returned to 0.1 Hz just after the
 142 load reduction. This new load was maintained and the displacement monitored until a positive
 143 displacement rate was clearly observed. The load was then gradually increased back to the original value
 144 at a similar loading rate as in the initial loading increment. The load was then held constant until a steady-
 145 state displacement rate was again achieved, which was typically within a factor of two of the steady-state
 146 rate achieved in the first loading step. This cycle of load reduction followed by a return to the original
 147 load was carried out multiple times in each experiment. In each cycle, the load was reduced a greater
 148 amount than in the previous cycle, but after each load reduction, the load was always returned to the
 149 original control value. For several experiments, this progression of load reductions was repeated to test
 150 the reproducibility of the sample response. An overview of the experimental conditions are provided in
 151 Table 1.

Sample # Experiment #	Loading direction	Temperature (°C)	Initial stress (MPa)	Total strain (%)	Steady-state strain rate (10^{-5} s^{-1})	Best-fit backstress (MPa)	Best-fit hardening coefficient, γ	Transient	Symbol in figures
OxR0002 170120c	[101] _c	1250	162	17%	3.76	84	14	inverse	■

OxR0007 170323	[110] _c	1250	189	12%	5.81	102	28	inverse	▶
OxR0009 170616	[110] _c	1300	105	17%	1.95	64	12	unclear	◀
OxR0009 171018	[110] _c	1300	77	38%	1.31	39	5	inverse	△
OxR0010 171016	[011] _c	1300	116	13%	0.12	104	55	normal	○

152

153 Experiments were stopped after an increment of deformation at the original load value. This final load
 154 value was maintained until steady-state displacement rates were obtained so that the preserved
 155 microstructure best reflects the microstructure just prior to each load reduction. At this point, the load was
 156 removed entirely from the sample and the furnace was shut off. Cooling to ambient temperature required
 157 several hours, but temperatures fell below 800°C in ~3 min, which is rapid enough to preserve the
 158 microstructures characteristic of the highest stresses applied (Bai and Kohlstedt 1992b; Goetze and
 159 Kohlstedt 1973).

160 ***2.3 Microstructural analysis***

161 For one experiment (OxR0009, compressed along [110]_c), the microstructures within the sample were
 162 characterized after two segments of deformation. The experiment was initially interrupted at 17% strain.
 163 At this point, the face parallel to (001) was polished with successively finer diamond grits down to a grit
 164 size of 50 nm, providing a polish suitable for EBSD. An initial EBSD map was collected in an area of
 165 high surface quality near the bottom of the polished vertical face of the sample. The sample was then
 166 reloaded into the apparatus and subjected to further increments of deformation. The experiment ended
 167 after a total of 38% strain. Two additional EBSD maps were collected on the same sample surface parallel
 168 to (001). One of these maps was located near the center of the sample and the other near a vertical edge.

169 The EBSD maps of sample OxR0009 were constructed using high-angular resolution electron backscatter
 170 diffraction (HR-EBSD). Data were acquired on an FEI Quanta 650 scanning electron microscope at the
 8

171 University of Oxford and a Philips XL30 scanning electron microscope at Utrecht University. Both
 172 instruments were equipped with an Oxford Instruments AZtec EBSD system and calibrated for HR-EBSD
 173 analysis by mapping undeformed Si standards following the procedure of Wilkinson et al. (2006). A
 174 routine to calibrate the chamber geometry, based on determining the pattern centre from diffraction
 175 patterns collected at a range of camera insertion distances, was performed before acquisition of each
 176 dataset. Conventions for reference frames in data acquisition and processing were validated using the
 177 approach of Britton et al. (2016). The details of each map are presented in Table 2.

Table 2: Details of HR-EBSD maps collected from sample OxR0009. The first map was collected after experiment 170616, and the subsequent maps were collected after experiment 171018. See Table 1 for details of the experiments.				
Total strain	Map location on sample surface	Step size (μm)	Number of points	Pixels in diffraction pattern
17%	Bottom edge	3.0	230 x 150	1344 x 1024
38%	Centre	0.3	300 x 250	1344 x 1024
38%	Side edge	0.5	230 x 160	1344 x 1024

178

179 Maps of lattice rotation and elastic strain heterogeneity were generated following the HR-EBSD post-
 180 processing method of Wilkinson et al. (2006) and Britton and Wilkinson (2011, 2012). 100 regions of
 181 interest in each diffraction pattern were cross correlated with a reference pattern chosen within each map.
 182 Shifts in the regions of interest were used to estimate the deformation gradient tensor, which was
 183 decomposed into rotations and strains (assumed to be entirely elastic) of the diffraction pattern, at each
 184 point in the map. The pattern remapping approach of Britton and Wilkinson (2012) allows residual elastic
 185 strain measurements in the presence of lattice rotations of several degrees. Stresses were estimated from
 186 the elastic strain measurements following the approach of Britton and Wilkinson (2012) and employing
 187 the elastic constants for olivine at room temperature from Abramson et al. (1997). Measured elastic

188 strains are relative to the unknown strain state of the reference point and therefore provide maps of stress
189 heterogeneity. We rotated measured stress tensors from the reference frame of the EBSD maps into the
190 reference frames of the measured crystal orientations to obtain the shear stresses resolved on each slip
191 system (David Wallis et al. 2017). A comprehensive overview of all data acquisition and processing
192 procedures for HR-EBSD is provided by Wallis et al. (2019).

193 **3 Results**

194 ***3.1 General creep behavior***

195 Figure 1 presents stress and strain as a function of time for the first 800 s of experiment 170616 with
196 sample OxR0009, which is a typical example of the response of all samples. In this particular experiment,
197 the strain rate did not significantly evolve, but was instead approximately constant over the first ~1% of
198 strain (120 to 200s in Figure 1). In other experiments, the strain rate after initial loading was observed to
199 decrease or increase with progressive strain before a steady-state strain rate was reached, which we refer
200 to as “normal” or “inverse” transients, respectively. Table 1 indicates the type of transient observed for
201 each experiment. Figure 1 also illustrates that, once a steady-state strain rate was clearly achieved, stress
202 reduction tests were executed. At the end of each reduction test, the stress was increased to approximately
203 the same value as the initial stress. During these high-stress intervals, the strain rate returned to a similar
204 strain rate to that just prior to the initial stress reduction.

205 Figure 2 compares the steady-state strain rate from each experiment to predictions of the flow laws for
206 single crystals of San Carlos olivine from Bai and Kohlstedt (1992a). These data are also reported in
207 Table 1. In general, samples loaded in the $[110]_c$, $[101]_c$, and $[011]_c$ orientations exhibit good agreement
208 with the flow-law predictions for olivine deformed at 1250°C and 1300°C. The maximum differences
209 between measured and predicted strain rates are on the order of a factor of two.

210 **3.2 Stress-reduction tests**

211 The results of individual stress-reduction tests are compiled in Figure 3. To obtain these data, we partition
212 each time series of strain into ranges spanning the point just before the stress reduction to the point just
213 before the stress was increased back to the initial stress. The strain at the beginning of this range (i.e., just
214 before the reduction) was set to 0, and the strain data were then corrected for the compliance of the
215 apparatus. This corrected strain after the stress reduction is presented as a function of time in the left
216 column of Figure 3. Small stress reductions result in a small elastic lengthening (negative strain) of the
217 sample that is immediately followed by continued shortening (positive strain). Large stress reductions
218 result in correspondingly large elastic lengthening of the sample, but that lengthening is followed by an
219 additional, time-dependent lengthening of the sample that we refer to as anelastic reverse strain. The
220 period of anelastic lengthening lasts for 10s to 100s of seconds depending on the magnitude of the stress
221 reduction.

222 We further analyze these data following the method of Blum and Finkel (1982). Many early analyses of
223 stress-reduction experiments (e.g., Ahlquist and Nix 1971) relied on measuring strain rates after the
224 anelastic reverse strain as a means to assess the “constant microstructure” mechanical behavior. Similar
225 methods have been applied to some geological materials such as ice (Caswell, Cooper, and Goldsby
226 2015). Unfortunately, strain rates are generally not constant during this increment of stress-reduction
227 tests, and therefore identifying the best segment for calculating a strain rate is not trivial. In contrast, the
228 method of Blum and Finkel (1982) does not rely on measuring strain rates but instead on measuring the
229 magnitude of anelastic reverse strain after the stress reduction and prior to subsequent forward creep. We
230 identify the total amount of reverse strain (both elastic and anelastic) using the minimum strain recorded
231 after the stress reduction. Based on the noise in the strain data, this selection process may overestimate the
232 total reverse strain by $\sim 10^{-4}$ (roughly 10% of the maximum anelastic reverse strain). We also identify the

233 elastic component of the reverse strain as the strain at the first data point after the reduced stress level is
234 reached.

235 The total and elastic reverse strains are presented for all experiments in the middle column of Figure 3.
236 For most experiments, the elastic strains are linearly correlated with the magnitude of the stress change
237 and in good agreement with the strains predicted given the Young's modulus in the specific crystal
238 orientation (dashed lines). Agreement with the elastic modulus provides confidence in the apparatus
239 correction and the method of identifying the elastic strain. However, for samples deformed at smaller
240 initial stresses, some elastic strains are smaller than predicted by the elastic modulus (e.g., OxR0009b and
241 OxR0010), which may indicate the apparatus compliance is overestimated at small loads.

242 We take the difference between the total reverse strain and the elastic reverse strain to represent the
243 anelastic reverse strain, which is plotted as a function of the magnitude of the stress reduction in the right
244 column of Figure 3. Crystals deformed in the $[110]_c$ and $[101]_c$ orientation exhibit maximum anelastic
245 reverse strains $>10^{-3}$, but significant anelastic reverse strain is only observed following stress reductions
246 greater than $\sim 40\%$ of the initial stress. In contrast, the crystal deformed in the $[011]_c$ orientation exhibits
247 anelastic reverse strains that gradually increase with the magnitude of the stress reduction, even for small
248 stress reductions.

249 ***3.3 Microstructures***

250 Figure 4 presents HR-EBSD maps of sample OxR0009. The dataset collected near the bottom edge of the
251 sample after deformation to 17% strain exhibits lattice rotations dominated by the ω_{12} component. The
252 map of this component exhibits a smooth gradient from the upper-right to lower-left, i.e., in the $[100]$
253 direction. For the mapped crystal orientation, the ω_{12} component corresponds to rotations around the
254 $[001]$ axis, and large magnitudes of that component are therefore consistent with the presence of

255 (010)[100] edge dislocations (David Wallis et al. 2016). Signal in the maps of the ω_{13} and ω_{23}
256 components has magnitudes many times lower than that of ω_{12} , precluding major contributions from other
257 dislocation types to the mapped lattice curvature. The map of shear stress resolved on the (010)[100] slip
258 system (i.e., σ_{ab}) also exhibits gradients in the [100] direction, varying by magnitudes on the order of 100
259 MPa over distances of a few hundred microns. The dataset collected from near the centre of the sample at
260 the final strain of 38% exhibits lattice rotations similar to those in the dataset collected at lower strain.
261 The stress distribution is homogeneous over the length scale of the map, which is notably smaller than
262 that collected at 17% strain. However, the dataset collected near a side edge of the sample at 38% strain
263 exhibits more discontinuous rotation and stress fields. Each component of the lattice rotation exhibits two
264 linear discontinuities corresponding to subgrain boundaries. The boundaries have traces parallel to [010]
265 and are most pronounced in the map of ω_{12} , consistent with them being dominated by (010)[100] edge
266 dislocations. The boundaries also coincide with discontinuities in the map of σ_{ab} . These stresses have the
267 greatest magnitudes, i.e., are localised, adjacent to the boundaries. Across the boundaries, the stresses
268 exhibit changes in sign and changes in magnitude on the order of 100 MPa. The orientation gradients
269 between the upper-right and lower-left corners of each map of ω_{12} correspond to average GND densities
270 in the range $4 \times 10^{11} \text{ m}^{-2}$ to $8 \times 10^{11} \text{ m}^{-2}$ (David Wallis et al. 2016). We emphasize that subgrain boundaries
271 are essentially not observed at low strains, and at high strains are only observed in small portions of the
272 sample.

273 **4 Discussion**

274 In this study we present results of stress-reduction tests carried out on single crystals of San Carlos
275 olivine. The key observations are: 1) prior to stress reductions, strain rates reach a steady state in
276 agreement with previously published flow laws for olivine, 2) after stress reductions of sufficient
277 magnitude, an anelastic reverse strain is observed, 3) the magnitude and duration of anelastic reverse

278 strain is a strong function of the magnitude of the stress reduction, 4) significant heterogeneity in the
279 residual stress is correlated with gradients in lattice orientation (i.e., with GNDs). To interpret these
280 observations, we first compare previously published interpretations of stress reduction tests to our data
281 and then reanalyze our data in the context of recent work on the plastic deformation of olivine.

282 ***4.1 Comparison to previous interpretations of stress-reduction tests***

283 Stress-reduction tests have been a common technique for investigating the microphysics of creeping,
284 crystalline materials. Two primary aspects of the microphysics have been investigated with stress
285 reduction tests. The first is the concept of a backstress (or internal stress), which is related to the details of
286 the microstructural evolution during deformation. The observation of backstress in single crystals
287 indicates that it arises from the long-range elastic interactions among dislocations. Dislocation arrays can
288 result in a net Burgers vector with a long-range internal stress field that opposes the macroscopically
289 applied stress, hence the term backstress. As described in detail by Bayley et al. (2006), the net backstress
290 associated with an array of dislocations is strongly dependent on the spatial gradients in dislocation
291 density, rather than simply the number of dislocations, and therefore the backstress is sensitive to the full
292 dislocation microstructure, including mobile dislocations, subgrain boundaries, and their spatial
293 distributions. The macroscopic creep rate is assumed to result from the action of an effective stress, σ_e ,
294 which is the difference between the externally applied stress and the net backstress, $\sigma_e = \sigma - \sigma_b$, where σ is
295 the former and σ_b is the latter. Macroscopic forward creep results from positive values of σ_e , and reverse
296 creep results from negative values of σ_e .

297 Early experiments on pure metals by Gibbs (1966), solid-solution alloys by Ahlquist and Nix (1971), and
298 ionic crystals by Menezes and Nix (1971) demonstrated that the average backstress could be determined
299 with stress-reduction tests (for a review, see Takeuchi and Argon 1976). In this method, the
300 microstructure and associated σ_b are presumed to remain constant during the nearly instantaneous stress

301 reduction. Just after the reduction, the immediate strain rate is observed to be positive, negative, or
302 approximately zero, depending on the magnitude of the stress reduction. These scenarios are presumed to
303 indicate that the applied stress after the reduction is either greater than, less than, or equal to the
304 backstress, respectively. Therefore, the reduced stress at which the subsequent strain rate is approximately
305 zero is taken to be equal to the backstress. However, there is some controversy about the practical aspects
306 of identifying a zero strain rate (for a review, see Nix and Ilschner 1979), and therefore we adopt the
307 method of Blum and Finkel (1982), as described above. In this latter method, the reduced stress at which
308 anelastic reverse strain becomes measurable is taken as equal to the average backstress.

309 These methods have been used to characterize net backstresses in a wide range of materials. Two well-
310 cited studies, in particular, had remarkably consistent results, estimating backstresses at 52% of the initial
311 stress in both pure metals (Evans, Roach, and Wilshire 1985) and solid-solution alloys (Blum and Finkel
312 1982). Many subsequent modeling efforts therefore have taken this value as a constant in the creep of
313 metals (e.g., Biberger and Gibeling 1995). Similar values have been observed in some ceramics such as
314 $\text{Gd}_3\text{Ga}_5\text{O}_{12}$ (Z. Wang, Karato, and Fujino 1996), which exhibited a backstress of 62% of the initial stress.
315 However, broader compilations of backstress estimates (Takeuchi and Argon 1976; Argon and Takeuchi
316 1981; Čadek 1987; Milička, Trojanová, and Lukáč 2007) demonstrate that the relationship between the
317 backstress and initial stress varies systematically as a function of the initial stress. For instance, Menezes
318 and Nix (1971) reported values of the backstress in LiF that vary systematically between 21% and 83%.
319 In addition, Wang et al. (1993) reported backstresses in SrTiO_3 up to ~100%.

320 The second aspect of the microphysics of creep investigated with stress reduction tests is the rate limiting
321 process at constant microstructure. As noted above, the specific dislocation arrangements are considered
322 to be unchanged (neglecting unbowing of dislocations) during the stress reduction. Therefore, in the case
323 that the stress reduction is small and no anelastic strain occurs, the forward strain rate just after the

324 reduction is a function of the same microstructure as before the reduction. A variety of studies (for a
325 review, see Biberger and Gibeling 1995) have evaluated these types of tests and found that the strain rates
326 after a stress reduction are fit well by a flow law with an exponential dependence of strain rate on the
327 stress, which is one member of a class of equations used to describe plastic deformation limited by the
328 glide velocity of dislocations (e.g., Kocks, Argon, and Ashby 1975; Weertman 1957). Furthermore, the
329 dependence of the strain rate on the reduced stress can be related to the apparent activation area of gliding
330 dislocations (the area of slip plane traversed in a single activation event), which was shown to have a
331 direct relationship to the observed spacing of free dislocations in subgrain interiors. These results led the
332 authors (and authors cited therein) to conclude that the strain rates directly after a load reduction are
333 dominated by the kinetics of gliding dislocations rate limited by the lattice friction (i.e., the Peierls-
334 Nabarro mechanism). Similar conclusions based on stress-reduction tests have been drawn for LiF
335 (Müller, Biberger, and Blum 1992), SrTiO₃ (Z. Wang, Karato, and Fujino 1993), and Gd₃Ga₅O₁₂ (Z.
336 Wang, Karato, and Fujino 1996).

337 The observations described above have played a large part in informing the development of composite
338 models to describe both transient and steady-state creep properties of crystalline materials. Key early
339 models include those proposed by Hart (1976), Nix and Ilschner (1979), and Mughrabi (1980), although a
340 variety of elaborations have been proposed (e.g., Korhonen, Hannula, and Li 1987; Garmestani, Vaghar,
341 and Hart 2001; Bammann 1989). The key features of these models are that 1) plastic deformation across a
342 wide range of conditions is effectively controlled by the glide of dislocations, 2) the glide velocity of
343 those dislocations is moderated by the long-range stresses associated with heterogeneity in the state
344 variables that describe the microstructure (what we refer to as a net backstress), and 3) the macroscopic
345 behavior can be modified by different recovery mechanisms (such as dislocation climb and annihilation)
346 that modify the backstress. We use these three concepts as a foundation for analyzing our data for olivine
347 in the next section.

348 ***4.2 Linking stress reductions to backstress evolution and dislocation-glide*** 349 ***kinetics***

350 Our working hypothesis based on the discussion above is that deformation after a stress reduction is
351 controlled by the glide of dislocations, and the anelasticity observed after larger stress reductions is
352 controlled by the net backstresses associated with the long-range stress fields of the dislocation
353 microstructure. Plastic deformation and the evolution of backstresses were recently investigated for
354 olivine by Hansen et al. (2019). In that work, the authors used experiments conducted at temperatures as a
355 low as room temperature to examine the yield strength and hardening behavior of single crystals and
356 polycrystalline samples of San Carlos olivine. Notably, the hardening behavior of single crystals is
357 indistinguishable from the hardening behavior of polycrystalline aggregates, which we interpret to
358 indicate that the dominant processes leading to strain hardening are intragranular. Furthermore, they
359 observed a distinct Bauschinger effect, which supports the conclusion that the hardening is associated
360 with long-range interactions of dislocations (see section 2.5 in Kassner 2015). This conclusion is further
361 supported by microstructural correlations of the GND density field with residual stress fields in the same
362 samples (David Wallis, Hansen, Kumamoto, et al. 2020). In support of the hypothesis that these long-
363 range stress fields are also important during deformation at high temperatures, we see spatial correlations
364 between lattice rotation gradients (i.e., GND densities) and stresses in our samples (Figure 4) and the
365 similar samples of Wallis et al. (2017). Furthermore, Wallis et al. (2020) highlighted the similarities
366 between stress fields in aggregates of olivine deformed at temperatures of 1150–1250°C and those
367 deformed at room temperature. These similarities include the magnitudes, the forms of the probability
368 distributions, and the characteristic length scales of the stress heterogeneity, along with a causative link to
369 GNDs in both temperature regimes.

370 *4.2.1 Magnitude of anelastic reverse strain*

371 To further analyze these data, we assess the magnitude of anelastic reverse strain after a stress reduction.
 372 We use the equations describing plasticity in olivine outlined by Hansen et al. (2019). The basic rate
 373 equation is derived following the classical treatment (e.g., Weertman 1957) and assumes the dislocation
 374 velocity is proportional to a Boltzmann distribution ($\exp\left[\frac{\Delta G}{RT}\right]$, where ΔG is the Gibbs free energy, R is the
 375 gas constant, and T is the temperature) describing the probability of the dislocation overcoming the
 376 energy barrier to its motion. Under application of a stress, ΔG becomes stress dependent. Hansen et al.
 377 (2019) used a common simplification that ΔG is a linear function of the applied stress, although we
 378 recognize that a variety of nonlinear relationships have been proposed to describe energy barriers, such as
 379 the lattice friction, of different shapes (chapter 4 in Caillard and Martin 2003; chapter 6 in Suzuki,
 380 Takeuchi, and Yoshinaga 2013; p. 141 in Kocks, Argon, and Ashby 1975). Additionally, Hansen et al.
 381 (2019) used \sinh instead of an exponential, which was originally proposed by Garofalo (1963), and later
 382 given physical justification by considering the potential for forward and backward fluctuations of the
 383 dislocation (Wu and Krausz 1994; Krausz 1968; Wilson and Wilson 1966). These considerations yield a
 384 flow law for the plastic strain rate from gliding dislocations, $\dot{\epsilon}_p$, of the form

$$\dot{\epsilon}_p = A_1 \exp\left(\frac{-\Delta F}{RT}\right) \sinh\left(\frac{\Delta F}{RT} \frac{\sigma - \sigma_b}{\Sigma}\right), \quad (1)$$

385 where A_1 is a constant with units of s^{-1} , ΔF is the activation energy, σ is the applied stress, σ_b is the
 386 backstress, and Σ is stress to overcome the barrier at 0 K. Equations of this form or similar can be used to
 387 describe a wide variety of barriers to dislocation motion, such as precipitates, forest dislocations, or grain
 388 boundaries in the general context of “low-temperature plasticity” (chapter 2 in Frost and Ashby 1982).
 389 However, in regards to creep of single crystals of olivine, we are primarily concerned with the barrier
 390 presented by the fundamental motion of dislocations through the lattice (aka, lattice friction or the Peierls-

391 Nabarro mechanism) by, for instance, the formation and migration of kink pairs. In this case, Σ is referred
 392 to as the Peierls stress.

393 As described above, the effective stress ($\sigma - \sigma_b$) determines the glide velocity of dislocations, and
 394 therefore any evolution of the strain rate during a test at constant stress results from the evolution of σ_b . It
 395 is important to note that $\dot{\epsilon}_p$ will be negative if $\sigma_b > \sigma$. Hansen et al. (2019) provided an evolution equation
 396 for σ_b ,

$$\frac{d\sigma_b}{d\epsilon_p} = \gamma[\sigma_{b,max} - \text{sgn}(\dot{\epsilon}_p)\sigma_b], \quad (2)$$

397 where γ is a rate constant and $\sigma_{b,max}$ is the maximum backstress. That is, if there is zero initial backstress,
 398 the initial rate of increase is given by $\gamma\sigma_{b,max}$, and the steady-state backstress is $\sigma_{b,max}$. Although they
 399 implemented this equation in an empirical manner, there are physical meanings to each of these terms
 400 (e.g., Mecking and Kocks 1981). Assuming the backstress is related to the dislocation density (e.g.,
 401 Taylor 1934), $\gamma\sigma_{b,max}$ is related to the dislocation nucleation rate, and γ is related to the dislocation
 402 recovery rate associated with dynamic recovery, which operates at high stresses and low temperatures. At
 403 elevated temperatures, additional recovery terms should be included to account for effects such as
 404 dislocation climb or grain-boundary migration. The explicit links between backstress evolution and the
 405 dislocation microstructure in olivine will be explored in future work.

406 An analytical solution exists for equation 2, providing the evolution of the back stress as a function of
 407 strain,

$$\sigma_b(\epsilon_p) = \text{sgn}(\dot{\epsilon}_p)\sigma_{b,max} + (\sigma_{b,0} - \text{sgn}(\dot{\epsilon}_p)\sigma_{b,max})\exp(-\gamma\epsilon_p\text{sgn}(\dot{\epsilon}_p)), \quad (3)$$

408 where $\sigma_{b,0}$ is the initial back stress. This equation can be rearranged to predict the total plastic strain
 409 necessary for σ_b to reach a final value, $\sigma_{b,f}$,

$$\varepsilon_p = [\text{sgn}(\dot{\varepsilon}_p)\gamma]^{-1} \ln \left[\frac{\sigma_{b,f} - \text{sgn}(\dot{\varepsilon}_p)\sigma_{b,\max}}{\sigma_{b,0} - \text{sgn}(\dot{\varepsilon}_p)\sigma_{b,\max}} \right]. \quad (4)$$

410 In the case of a large stress-reduction test, $\dot{\varepsilon}_p \dot{\sigma}_p \dot{\varepsilon}_p \dot{\sigma}_p \dot{\varepsilon}_p < 0$ just after the reduction. The backstress at the
 411 time of the reduction, $\sigma_{b,0}$, is some fraction, β , of the initial applied stress prior to the reduction, σ_i . After
 412 the reduction, the backstress will decrease until a value of $\sigma_{b,f}$ is reached. This final value cannot, by
 413 definition, be larger than the applied stress after the reduction, σ_r , and it will only reduce further than σ_r if
 414 some additional recovery process is involved, such as “static” annealing of the dislocation density (e.g.,
 415 annihilation by dislocation climb). Based on published static annealing rates for mobile dislocations in
 416 olivine (Toriumi and Karato 1978; S.-I. Karato, Rubie, and Yan 1993) as a proxy for relaxation of the
 417 backstress, estimates for the total recovery for the longest durations of anelastic strain (100s of seconds)
 418 range from <1% to ~10%. Therefore, we assume that static recovery is negligible during the anelastic
 419 portion of these experiments, and we expect that $\sigma_{b,f} = \sigma_r$ at the end of anelasticity and prior to subsequent
 420 forward creep. These considerations allow us to rewrite equation 4 for the maximum anelastic reverse
 421 strain after a stress reduction as $\dot{\varepsilon}_p$

$$\varepsilon_p = \frac{-1}{\gamma} \ln \left(\frac{\sigma_r + \sigma_{b,\max}}{\beta\sigma_i + \sigma_{b,\max}} \right). \quad (5)$$

422 Note that the assumption made above is only valid for the case in which anelastic reverse strain occurs
 423 (i.e., when $\sigma_r < \beta\sigma_i$). If the applied stress is not reduced below this threshold, then no anelastic reverse
 424 strain occurs (i.e., $\varepsilon_p = 0$).

425 Equation 5 can be compared to our experimental data to find values for key parameters. We assume that
426 $\sigma_{b,max} = 1.8$ GPa according to the results of our experiments at low temperatures (Hansen et al. 2019). We
427 then compare the measured anelastic reverse strains for large stress reductions to equation 5 to find the
428 best-fit values of γ and β (and therefore the backstress prior to the stress reduction from equation 4).
429 Values for these parameters are presented in Table 1 and a comparison of equation 5 to anelastic reverse
430 strains is presented in Figure 5.

431 These results indicate that, in olivine deformed in the $[110]_c$ and $[101]_c$ orientations, the magnitudes of
432 anelastic reverse strain are consistent with backstresses between 48 and 61% of the initially applied stress,
433 which are largely consistent with most previously reported values in other materials (see section 4.1
434 above). Interestingly, our results for olivine deformed in the $[011]_c$ orientation suggest that the backstress
435 is nearly equal to the applied stress. This difference in backstress between different crystal orientations,
436 and therefore between different activated slip systems, is likely a result of different rates of dislocation
437 recovery, as will be explored later in this section.

438 The values of the best-fit rate constant, γ , also differ between crystal orientations. Olivine deformed in the
439 $[110]_c$ and $[101]_c$ orientations is characterized by values of γ between 5 and 28. However, olivine
440 deformed in the $[011]_c$ orientation is characterized by a value of γ of 55, suggesting some anisotropy in
441 the hardening behavior. The former values are considerably smaller than the value of $\gamma = 75 \pm 20$
442 determined in low-temperature experiments (Hansen et al. 2019). However, the value of $\gamma = 55$ for the
443 crystal deformed in the $[011]_c$ orientation is within error of that determined in previous experiments.
444 Those previous experiments examined both polycrystalline aggregates and single crystals, but only single
445 crystals in the $[011]_c$ and $[111]_c$ orientations were investigated, and both orientations should have a large
446 part of the dislocation content on the $(010)[001]$ slip system. Therefore, at least where comparisons can be
447 made, this analysis of the anelastic reverse strain is consistent with the same mechanism of deformation

448 being responsible for transient deformation at low and high temperatures, as suggested by the
449 microstructural interpretations of Wallis et al. (2020). Furthermore, these results provide initial evidence
450 that transient deformation on the strongest slip system may dominate the transient response of a
451 polycrystalline sample, which is inconsistent with some recent theoretical treatments of transient creep in
452 olivine suggesting the transient is controlled by the weakest slip system (Masuti et al. 2019).

453 *4.2.2 Strain rates immediately after a stress change*

454 If the physics of backstress associated with dislocation interactions (equation 2) can explain the
455 magnitude of the anelastic reverse strain, then following from previous treatments for metals (e.g.,
456 Biberger and Gibeling 1995), we hypothesize the physics of dislocation glide can explain the strain rates
457 observed just after a change in stress. This hypothesis is similar to the suggestion by Cooper et al. (2016)
458 that load relaxation experiments on olivine single crystals are rate limited by the glide of dislocations. We
459 plot strain rates just after our stress reductions in Figure 6a as a function of the effective stress, σ_e , which
460 was determined by subtracting the value of σ_b determined in Figure 5 from the reduced stress. In other
461 words, we suggest these stresses and strain rates in Figure 6a reflect the rheological behavior of olivine
462 when no backstress is present. Only strain rates for small stress reductions without any measurable
463 anelastic reverse strain are presented. Strain rates from the crystal deformed in the $[011]_c$ direction are not
464 plotted because all tests for that sample exhibit some anelasticity. The observed strain rates are
465 consistently faster than the strain rates predicted for steady-state creep, and interestingly, the apparent
466 power-law exponent is ~ 1 . This observation may initially seem at odds with the hypothesis that creep at
467 “constant microstructure” is controlled by the glide of dislocations. However, as recently discussed in the
468 context of olivine deformation by Cooper et al. (2016), the apparent stress exponent of an exponential
469 flow law decreases with decreasing stress, and therefore, these data could indeed be explained by an
470 exponential function. In fact, the sinh function employed by Hansen et al. (2019) and described in
471 equation 1 results in a linear relationship between strain rate and effective stress at low stresses.

472 We also compare these strain rates to data from previously published experiments at high temperatures in
473 Figure 6b. To do so, we need data from experiments in which the backstress, and therefore the effective
474 stress, is known. We suggest that the strain rates just after initial loading of constant-stress experiments
475 reasonably represent a case in which the backstress is zero since very little strain has accumulated to
476 produce a backstress. Data of this type are available for single crystals of San Carlos olivine (Hanson and
477 Spetzler 1994; Cooper, Stone, and Plookphol 2016) and polycrystalline aggregates of San Carlos olivine
478 (Chopra 1997). We also include the yield stresses from single crystals deformed at room temperature at
479 constant strain rate (Hansen et al. 2019). A complication in comparing data from the first increments of
480 strain in constant-stress (or constant-strain-rate) tests is that the initial strain rate (or stress) is likely highly
481 sensitive to the density of mobile dislocations present in the starting material. Therefore, we normalize the
482 strain rates in Figure 6b by the dislocation density at the beginning of the measurement. For our data, the
483 initial dislocation density is calculated from the initial stress before the reduction using the dislocation-
484 density piezometer of Bai and Kohlstedt (1992b). The initial values of dislocation density in the previous
485 studies noted above are not available, but we estimate the starting density of single-crystal samples as 10^{10}
486 m^{-2} based on observations in untreated San Carlos olivine (Toriumi and Karato 1978) and of
487 polycrystalline samples as 10^{12}m^{-2} based on observations of hot-pressed Anita Bay dunite (S.-I. Karato,
488 Paterson, and FitzGerald 1986).

489 The comparison in Figure 6b provides two key observations. First, the apparent stress exponent differs for
490 each individual data set, systematically increasing with increasing stress. This observation is consistent
491 with deformation just after a stress reduction being controlled by the glide of dislocations following an
492 exponential or sinh flow law. Second, we also plot the flow law from Hansen et al. (2019) (equation 1 and
493 dashed lines in Figure 6b). This flow law does well at predicting the strain rates in the room-temperature
494 experiments on which the flow law is based, but does poorly at predicting the strain rates at high
495 temperatures. The flow law overpredicts strain rates from this study by approximately six orders of

496 magnitude. This discrepancy at high temperatures is not that surprising since the temperature-dependence
 497 is the most poorly constrained component of the flow law. Not only was the flow law primarily calibrated
 498 with data collected at room temperature, but data at higher temperatures were either subject to low
 499 resolution in temperature measurement or were taken from other studies conducted with different
 500 methods. Furthermore, the apparent temperature dependence of equation 1 depends strongly on the
 501 assumption that the activation energy for glide is linearly dependent on stress. A nonlinear dependence, or
 502 even a transition in the dependence as a function of temperature is possible (chapter 4 in Caillard and
 503 Martin 2003). Therefore, we suggest that (1) our data are *consistent* with transient deformation being
 504 controlled by the process of dislocation glide but that (2) existing flow laws for glide-controlled plasticity
 505 in olivine need to be recalibrated before extension to such high temperatures.

506 4.2.3 Recalibration of the flow law for dislocation glide

507 Here we recalibrate the flow law for dislocation glide in olivine using the data presented in Figure 6b.
 508 However, we must modify equation 1 to reasonably apply this flow law to the range of data in Figure 6b,
 509 which covers a temperature range from 20°C to 1300°C. Although the form of the flow law calibrated by
 510 Hansen et al. (2019) was derived from the Orowan equation (see their equation 6), the density of mobile
 511 dislocations that actually produce strain was assumed to be relatively constant and therefore was
 512 incorporated into A_1 . This assumption is generally justified for applications to low-temperature, high-
 513 stress deformation because the stress dependence of the sinh term far outweighs the stress dependence of
 514 the mobile dislocation density. However, this is not necessarily the case at high temperatures or low
 515 stresses, and therefore we suggest a more robust form of the flow law as

$$\varepsilon_p = A_2 \rho \exp\left(\frac{-\Delta F}{RT}\right) \sinh\left(\frac{\Delta F}{RT} \frac{\sigma - \sigma_b}{\Sigma}\right), \quad (6)$$

516 where A_2 is a constant and ρ is the density of mobile dislocations. As with equation 1, this flow law
517 inherently assumes a linear dependence of ΔG on the effective stress (see section 4.2.1). A nonlinear
518 relationship may better characterize the fundamental physics of dislocation glide in olivine, but as
519 demonstrated by Jain et al. (2017)

520 Figure 6b compares our compiled data for strain rates controlled by dislocation glide to a best fit to
521 equation 6. In the applied fitting procedure, we fixed $\Sigma = 3.1$ GPa, which is well constrained by the
522 previous calibration using low-temperature data, and conducted a grid search to find the optimum values
523 of A_2 and ΔF . The best-fit values of these parameters are $A_2 = 10^{11.1 \pm 0.2} \text{ m}^2 \text{ s}^{-1}$ and $\Delta F = 827 \pm 20$ kJ/mol.
524 This value for ΔF is much higher than most previous estimates for dislocation glide flow laws in olivine,
525 which are generally between 300 and 600 kJ/mol (see the compilation by Demouchy et al. 2013). Our
526 choice of a linear relationship between ΔG and effective stress likely biases the best-fit activation energies
527 to high values. One outlier of previous work is an estimate of 1480 kJ/mol from Long et al. (2011)

528 Although our calibrated flow law uses a simplified form, at least empirically it is able to capture the
529 observed behavior over a wide range in temperatures, reasonably predicting both the magnitudes of the
530 strain rates as well as the change in the apparent stress exponent as a function of temperature.
531 Furthermore, combining equation 6 with a parameterization of the backstress evolution, such as that in
532 equation 2, allows the complete transient to be predicted. Different values of γ can be used to predict the
533 transient behavior of different slip systems, as discussed in relation to Figure 5. However, we note that
534 the dislocation recovery mechanisms implicit in equation 2 are only calibrated for use at low
535 temperatures. Therefore, prediction of the steady-state strain rates at elevated temperatures requires high-
536 temperature recovery mechanisms (e.g., dislocation climb) to be accounted for. Incorporating these
537 recovery mechanisms into a parameterization of dislocation creep in olivine will be a key topic addressed
538 in future work.

539 We can, however, assess the magnitude of the backstresses at high temperature. To restate the discussion
 540 above, we suggest that equation 6 controls the macroscopic strain rate in both transient and steady-state
 541 creep, and the evolution between the two regimes reflects the evolution of the net backstress. In this
 542 framework, at steady state, the steady-state strain rate would be equal to equation 6, which allows us to
 543 solve for the backstress at steady state,

$$\sigma_b = \sigma - a \sinh \left[\frac{\dot{\varepsilon}_{ss}}{A_2 \rho} \exp \left(\frac{F}{RT} \right) \right] \frac{RT \Sigma}{F}, \quad (7)$$

544 where $\dot{\varepsilon}_{ss}$ is the steady-state strain rate. In Figure 7, we present values of the steady-state back stress
 545 estimated with equation 7. These values were calculated using steady-state strain rates predicted by the
 546 flow laws for single-crystal olivine from Bai and Kohlstedt (1992a) and dislocation densities predicted by
 547 the dislocation-density piezometer from Bai and Kohlstedt (1992b). These calculated backstresses
 548 compare favorably to those observed in stress-reduction tests, which provides further confidence in our
 549 calibration of equation 6 and in our suggestion that equation 6 can be used to predict the steady-state
 550 strain rate if the backstress is known.

551 Notably, the calculated curves in Figure 7 capture the orientation dependence of the backstress. Equation
 552 7 correctly predicts that crystals compressed along $[011]_c$ have a backstress nearly equal to the applied
 553 stress, and that crystals deformed in other orientations have a backstress that is approximately 50% of the
 554 applied stress. Because we use the same values of A_2 , F , and Σ regardless of orientation, the orientation
 555 dependence of the calculated backstress results entirely from the different steady-state flow laws.
 556 Therefore, there is a clear link between the anisotropy of the steady-state creep rate and the anisotropy of
 557 the backstress evolution, which we suggest is primarily a reflection of anisotropic rates of dislocation
 558 recovery (e.g., L. Wang et al. 2016). We reiterate and emphasize that, although we propose dislocation

559 creep during the transient and steady state is governed by equation 6, the steady-state strain rate can still
560 be set by the kinetics of dislocation climb that counteract the buildup of additional backstress.

561 *4.2.4 Implications for the type of transient creep and load relaxation*

562 Our hypothesis linking low-temperature plasticity, transient creep, steady-state creep, and the evolution of
563 backstress predicts several other phenomena. A key phenomenon is variation in the sign of the strain
564 acceleration during the transient. That is, whether or not the strain rate decreases (a “normal” transient) or
565 increases (an “inverse” transient) during the evolution to steady state. Hanson and Spetzler (1994)
566 observed that the type of transient depends on the crystal orientation, and Cooper et al. (2016) observed a
567 transition in the type of transient in the same experiment as the applied stress was increased in steps.
568 Figure 8a schematically describes how the model presented here can predict both types of transients. We
569 suggest that the strain rates for olivine will generally be described by the flow law for dislocation glide
570 (equation 6). After initial application of stress to the sample, the mobile dislocation density and backstress
571 evolve toward their steady-state values. This change in the microstructural parameters shifts the flow law
572 to higher or lower strain rates until a steady state is reached. Thus, we hypothesize that the apparent
573 steady-state power law is fundamentally defined by the relationship between the steady-state backstress
574 and the applied stress. At the onset of deformation, if the dislocation-glide flow law predicts faster strain
575 rates than the steady-state strain rate, then the initial strain rate will be fast, and the flow law will
576 gradually shift to slower rates (a normal transient) due to an increasing backstress. Conversely, if the
577 initial strain rate dictated by the flow law is slower than at steady-state, the flow law will shift to faster
578 rates (an inverse transient) due to an increase in the density of mobile dislocations. Therefore, we suggest
579 that the intersection of the dislocation-glide flow law and the steady-state power law can be used to
580 predict whether normal or inverse transients will occur. Figure 8b presents the type of transient predicted
581 by this method over a range of temperatures and pressures for all three orientations of olivine. The

582 predictions are in excellent agreement with observations in this study (Table 1), as well as with the
583 observations made by Hanson and Spetzler (1994) and Cooper et al. (2016) .

584 We additionally note that, while this analysis correctly predicts a normal transient for the initial loading of
585 olivine along $[011]_c$, it also predicts that once steady state is reached, any subsequent stress increase
586 would lead to an inverse transient. Therefore, this model also correctly predicts the change in the type of
587 transient from normal to inverse observed by Cooper et al. (2016) in progressive load-stepping
588 experiments (see their Figure 4a).

589 We finally point out that our model is similar to that developed by Stone (1991) (in turn, fundamentally
590 inspired by the phenomenological theory of Hart (1970)) and applied to geological materials such as
591 halite (Stone, Plookphol, and Cooper 2004) and olivine (Cooper, Stone, and Plookphol 2016). Stone
592 (1991) describes a “master curve” or equation of state relating stress, strain rate, and the hardness, which
593 is a state variable related to the aspects of the microstructure that control the material response. The
594 “master curve” described by that model is analogous to the flow law presented here. The key difference
595 lies in the choice of microstructural variable that controls the hardness and translates the master curve in
596 stress–strain-rate space. Stone advocates that the self-similar nature of the microstructure in creeping
597 materials, which involves many different length scales, allows the essential aspects of that distribution to
598 be described by a single state variable. Stone uses the subgrain size as that variable. Instead, here we use
599 the net backstress as a representation of the full dislocation microstructure, which includes the stress
600 fields associated with subgrain boundaries. This distinction is important because the backstress is a more
601 general description of the microstructure and therefore can be applied to our samples, which generally do
602 not include appreciable subgrain boundaries.

603 An additional difference between the model of Stone (1991) and that presented here lies in the nature of
604 the relationship between the microstructural variable and the master curve. The master curve of Stone

605 (1991) represents, at high stresses, a plastic yield stress controlled by the subgrain size, and at low
606 stresses, a flow law describing Nabarro-Herring creep among subgrains. The transition of Stone's master
607 curve to Nabarro-Herring creep at low stresses was inspired by strain rates during load relaxation that
608 approached a linear relationship with stress. The flow law presented here results in a similar
609 phenomenological response, which includes, at high stresses, an exponential dependence of strain rate on
610 effective stress, and at low stresses, a linear dependence of strain rate on effective stress. In our model,
611 this full range of behavior results from a single flow law due to the nature of the sinh term in equation 6.
612 The model of Stone (1991) explains load-relaxation data for halite exceptionally well (Stone, Ploorkhol,
613 and Cooper 2004), collapsing the data set to a master curve when scaled by the subgrain size. In contrast,
614 in load relaxation experiments on single crystals of olivine in the $[011]_c$ orientation, Cooper et al. (2016)
615 found that the master curve is not shifted by the subgrain size. In fact, they demonstrated that the load-
616 relaxation response is unchanged by the initially applied stress and any associated changes in
617 microstructure, always falling on the same stress-strain-rate curve. Therefore, Cooper et al. (2016)
618 suggested that a different physical process controls the relaxation response of olivine, dislocation glide
619 with kinetics described by an exponential flow law. Our data and analysis provides an alternative, but
620 related, explanation that can be applied to both halite and olivine in load-relaxation experiments.

621 As described by equation 6, the backstress shifts the dislocation-glide flow law in stress-strain-rate space.
622 Figure 7 illustrates that the backstress for crystals deformed in the $[011]_c$ orientation is essentially equal to
623 the applied stress. This observation suggests that, during the initial evolution to steady state, the
624 backstress reaches a value equal to the applied stress before the flow law can shift to lower rates to reach
625 the steady-state rate. Therefore, during a load-relaxation experiment, the effective stress is initially zero,
626 and forward strain only proceeds due to the reduction of the backstress associated with dislocation
627 recovery. The need for recovery implies that load-relaxation in this context is not a constant
628 microstructure test, and indeed Cooper et al. (2016) observed a reduction in dislocation density during

629 relaxation. Continued forward strain and reduction of backstress would occur in lock step and simply
630 follow the steady-state power law regardless of the initial stress, again consistent with the observation of
631 Cooper et al. (2016). In contrast, for halite (Gupta and Li 1970) and other orientations of olivine (Figure
632 7), the backstresses are a smaller portion of the applied stress, and therefore the effective stress is both
633 finite and a function of the applied stress. In this context, a stress relaxation experiment would follow the
634 low-temperature plasticity flow law prior to any relaxation of the backstress. Therefore, we predict that
635 stress relaxation experiments conducted on other orientations of olivine would exhibit a similar response
636 as halite, following the flow law for dislocation glide and dependent on the magnitude of the initial stress.

637 ***4.3 Consequences for transient creep in the upper mantle***

638 Rheological models employed to analyze geodynamic scenarios vary widely in their form and behavior.
639 In terms of models that capture transient behavior, by far the most common is the Burgers model, which
640 contains two viscous elements, one describing the initial viscosity at the onset of loading and the other
641 describing the steady-state viscosity. Burgers models (and related variations including multiple anelastic
642 elements) have been calibrated for deformation of olivine dominated by diffusive mass transfer (Sundberg
643 and Cooper 2010; e.g., Faul and Jackson 2005) and by dislocation motion (Chopra 1997). The former
644 result in a linear viscoelastic model for which the viscosities do not depend on the level of stress applied,
645 whereas the latter result in nonlinear viscoelastic models for which the viscosities are stress dependent.
646 Linear viscoelastic models based on a Burgers model have been widely applied to a range of phenomena
647 including glacial isostatic adjustment (Yuen et al. 1986; e.g., Rumpker and Wolff 1996), postseismic
648 creep (e.g., Hetland and Hager 2005; Pollitz, Bürgmann, and Banerjee 2006), tidal dissipation (e.g.,
649 Nimmo, Faul, and Garnero 2012; Nimmo and Faul 2013; Bierson and Nimmo 2016), and seismic
650 attenuation (Carcione et al. 2014; S.-I. Karato 2012). Linear Burgers models have likely seen application
651 to such a wide range of processes because of the relative mathematical ease of their implementation and

652 the recognition that nonlinear viscoelasticity is generally restricted to large stress and strain amplitudes,
653 whereas most of these processes involve small stresses. However, nonlinear viscoelastic models have
654 seen increasing application to scenarios with larger stress changes, especially postseismic creep (Freed,
655 Hirth, and Behn 2012; Masuti et al. 2016). The viscosities in these nonlinear models are assumed to
656 follow power laws, motivated by the power-law behavior of olivine during steady-state dislocation creep.
657 However, the stress dependence is assumed to be the same for both the initial and the steady-state
658 viscosity. Therefore, in both linear Burgers models and nonlinear variations for upper mantle rocks, the
659 ratio of the initial and steady-state viscosities is generally taken to be a constant.

660 Our results and analysis presented above demonstrate that the rheological behavior of olivine can be quite
661 different than the behavior implemented in previous modelling efforts. As demonstrated by our data in
662 Figure 6 and illustrated schematically in Figure 8a, during initial loading, we predict the strain rate of
663 olivine to be close to linearly dependent on the stress at low stresses, with increasingly higher sensitivities
664 to stress with increasing stress (Figure 6b also illustrates that the transition between linear and nonlinear
665 behavior is not particularly dependent on temperature). Therefore, we predict the nonlinearity of the
666 initial viscosity to be a function of the stress. This conclusion is particularly noteworthy because, for
667 example, the apparent viscosity associated with geodynamic phenomena on short timescales could
668 potentially follow linear viscoelastic behavior even when dislocation glide is the main strain producing
669 process. Furthermore, if the nonlinearity of the initial viscosity is dependent on stress and temperature,
670 then the ratio of the initial viscosity to the steady-state viscosity will also be a function of the stress.

671 We note that the transient deformation behaviour of rocks may be subject to additional effects not
672 captured in our experiments on single crystals, including grain-boundary strengthening (Hansen et al.
673 2019; Kumamoto et al. 2017), recovery from grain-boundary migration (e.g., Toriumi 1982), stress
674 transfer between grains (Duval, Ashby, and Anderman 1983; Masuti et al. 2019), additional deformation

675 mechanisms, and the effects of other minerals and/or fluids. Nonetheless, the dislocation-mediated
676 processes that we analyse here should be ubiquitous across relevant geological conditions regardless of
677 the occurrence of other effects. Therefore, the model that we present provides a fundamental starting
678 point for analysing transient creep that allows isolation of the contribution from intragranular processes,
679 with the benefit that departures from such behaviour in polycrystalline or polyminerallic materials may
680 constrain contributions from additional processes.

681 **5 Conclusions**

682 Here we present a series of deformation experiments to investigate the microphysical mechanisms
683 controlling transient creep in olivine. We conducted stress-reduction tests on olivine single crystals at
684 elevated temperatures in a variety of crystal orientations. Our results reveal that stress-reductions are
685 often accompanied by anelastic reverse strain. The magnitude of the reverse strain is dependent on the
686 magnitude of the stress reduction. In certain crystal orientations, small stress reductions result in no
687 reverse strain, indicating that a backstress is present in the crystals that is a fraction of the initially applied
688 stress.

689 We recognise that deformation of olivine is fundamentally controlled by the glide velocity of dislocations,
690 and therefore hypothesize that a flow law based on the kinetics of dislocation glide can be applied across
691 a wide range of temperatures. The buildup of backstresses associated with strain hardening in low-
692 temperature plasticity is quantitatively consistent with the magnitudes of observed reverse strains. This
693 hypothesis also predicts that the strain rates just after a stress reduction can be predicted with a flow law
694 calibrated at low temperatures, however, the existing flow law considerably overpredicts the strain rates
695 observed here. Therefore, we recalibrate the activation energy of the flow law to be consistent with initial
696 strain rates in our experiments, initial strain rates in previously published high-temperature experiments,
697 and yield stresses in low-temperature experiments.

698 We suggest that this recalibrated flow law can be used to predict the transient and steady-state creep strain
699 rates by taking into account the evolution of the backstress and dislocation density. By combining the
700 recalibrated flow law with previously published flow laws for the steady-state creep of olivine single
701 crystals, we are able to correctly predict the magnitude of the observed backstress and its orientation
702 dependence. We are also able to predict whether strain rates decrease (normal) or increase (inverse)
703 during transient creep in our experiments and previously published experiments. This model also provides
704 an explanation for the results of previous stress-relaxation experiments.

705 The results and analysis presented here indicate that the rheological behaviour of olivine during transient
706 creep is fundamentally different from that incorporated into analyses of geodynamic processes. We
707 suggest that the initial viscosity after a stress change, if controlled by dislocations, can range from linear
708 to nonlinear, depending on the stress magnitude. Therefore, the ratio between the transient and steady-
709 state viscosities is likely a function of the stress.

710 **Acknowledgements**

711 The authors benefited greatly from conversation with H. Jay Melosh on the rheological behavior of
712 planetary bodies. His passing represents a great loss to our community. The authors would also like to
713 acknowledge fruitful discussions with Greg Hirth, Ben Holtzman, and David Kohlstedt. The manuscript
714 was greatly improved by constructive and thoughtful reviews from Reid Cooper and Brian Evans. LH and
715 DW acknowledge support from the Natural Environment Research Council, grant NE/M000966/1, LH
716 and CT acknowledge support from the Natural Environment Research Council, grant 1710DG008/JC4,
717 and DW acknowledges support from the Netherlands Organisation for Scientific Research, User Support
718 Programme Space Research, grant ALWGO.2018.038, and startup funds from Utrecht University. LH
719 recognizes funds used to develop the uniaxial apparatus from the John Fell Fund at the University of

720 Oxford. All data used in this study are available from the University of Minnesota Digital Conservancy
 721 (<http://conservancy.umn.edu>).

722 **Figure Captions**

723 Figure 1: Axial strain and stress as functions of time for the first 800 s of deformation of sample
 724 OxR0009. Seven stress reductions are illustrated after the primary loading phase. The initial stress used to
 725 set the microstructure was 105 MPa. After each stress reduction, the reverse strain was composed of both
 726 an elastic and an anelastic component, as denoted by annotations. Elastic strains in this figure are a
 727 combination of the elastic distortion of both the apparatus and the sample.

728 Figure 2: Comparison between strain rates from the steady-state portions of the experiments and
 729 published flow laws for single crystals of San Carlos olivine. Symbols represent data from this study
 730 (following Table 1), and lines represent flow laws from Bai and Kohlstedt (1992a). Color indicates crystal
 731 orientation and symbol indicates experiment. Open symbols and dashed lines indicate a temperature of
 732 1300°C, and filled symbols and solid lines indicate a temperature of 1250°C.

733 Figure 3: Compilation of data from all stress-reduction tests. (left) Strains after each reduction are aligned
 734 and plotted in grayscale. The grayscale indicates the order of the reductions, with darker colors indicating
 735 stress reductions earlier in the experiment. (middle) Magnitude of the stress reduction as a function of the
 736 strain after the reduction. Small markers indicate the elastic reverse strain, and larger markers indicate the
 737 total reverse strain. The dashed line indicates the Young's modulus for each crystal orientation based on
 738 the data of Abramson et al. (1997). (right) The anelastic reverse strain as function of the magnitude of the
 739 stress reduction. Anelastic reverse strains are calculated as the difference between large markers and
 740 small markers in the middle column. Marker shapes and colors are as designated in Table 1.

741 Figure 4: HR-EBSD maps of sample OxR0009, which was compressed in the $[110]_c$ orientation indicated
 742 in the pole figure, at different strains and locations in the sample annotated on the left. Lattice rotations
 743 (ω_{ij}) and shear stress on the $(010)[100]$ slip system (σ_{ab}) are relative to the orientation and stress state,
 744 respectively, of the reference points marked in black. The greyed-out areas in the top stress map indicate
 745 regions where the stress measurements are unreliable due to the large distances and large lattice rotations
 746 relative to the reference point.

747 Figure 5: Anelastic reverse strain as a function of the magnitude of the stress reduction at two different
 748 temperatures. Marker shapes and colors are as designated in Table 1. Solid lines are fits to equation 5.
 749 Only data with clearly measurable anelastic reverse strain are included in fits.

750 Figure 6: Analysis of strain rates measured immediately after stress reductions. (a) Strain rates measured
 751 after small reductions for which no anelastic reverse strain was detected. Stresses are effective stresses,
 752 that is, the applied stress minus the measured backstress given in Table 1. Marker shapes and colors are as
 753 designated in Table 1. Dashed and solid lines are flow laws for single crystals of olivine from Bai et al.
 754 (1991). (b) Strain rates as in (a) compared to previously published data. Strain rates from previous high-
 755 temperature creep tests (Hanson and Spetzler 1994; Cooper, Stone, and Plookphol 2016; Chopra 1997)
 756 were taken from the beginning of experiments in which the backstress is expected to be negligible. Data
 757 from Hansen et al. (2019) are yield stresses measured in constant-strain-rate experiments. Dashed lines

758 represent the flow law from Hansen et al. (2019). Solid lines represent the flow law calibrated in this
759 study.

760 Figure 7: Measured and predicted backstresses as a function of the applied stress. Markers indicate
761 backstresses determined using the analysis presented in Figure 5. The two thin black lines are guides for
762 values of backstress equal to the applied stress (1:1) or half of the applied stress (1:2). The curves are
763 backstresses predicted from equation 7.

764 Figure 8: Evaluation of the proposed model in the contexts of the shape of the transient and of stress
765 relaxation. (a) Schematic description of our model. The initial stress applied to a sample leads to a strain
766 rate controlled by flow law for dislocation glide (equation 6) without any backstress. If this strain rate is
767 higher than the steady-state strain rate, we predict that the transient will be normal and controlled by the
768 increase in backstress. If this strain rate is lower than the steady-state strain rate, we predict that the
769 transient will be inverse and controlled by the increase in density of mobile dislocations. In this
770 schematic, the backstress is assumed to always be less than the minimum stress on the plot. (b)
771 Conditions leading to inverse or normal transients calculated with the concept presented in (a). Data for
772 comparison come from the initial strain rates at the start of experiments presented by Cooper et al. (2016),
773 Hanson and Spetzler (1994), and this study. (c) Schematic prediction of different responses during stress
774 relaxation experiments. If steady state is reached before the backstress equals the applied stress, then
775 subsequent relaxation will follow the flow law. If the backstress increases to equal the applied stress at the
776 steady state, then subsequent load relaxation only results in forward strain as the backstress relaxes,
777 following the steady-state power law.

778 References

- 779 Abramson, E. H., J. M. Brown, L. J. Slutsky, and J. Zaugg. 1997. “The Elastic Constants of San Carlos
780 Olivine to 17 GPa.” *Journal of Geophysical Research, [Solid Earth]* 102 (B6): 12253–63.
- 781 Ahlquist, C. N., and W. D. Nix. 1971. “The Measurement of Internal Stresses during Creep of Al and Al-
782 Mg Alloys.” *Acta Metallurgica* 19 (4): 373–85.
- 783 Argon, A. S., and S. Takeuchi. 1981. “Internal Stresses in Power-Law Creep.” *Acta Metallurgica*.
784 [https://doi.org/10.1016/0001-6160\(81\)90113-9](https://doi.org/10.1016/0001-6160(81)90113-9).
- 785 Bai, Quan, and D. L. Kohlstedt. 1992a. “High-Temperature Creep of Olivine Single Crystals III.
786 Mechanical Results for Unbuffered Samples and Creep Mechanisms.” *Philosophical Magazine A* 66
787 (6): 1149–81.
- 788 ———. 1992b. “High-Temperature Creep of Olivine Single Crystals, 2. Dislocation Structures.”
789 *Tectonophysics* 206 (1): 1–29.
- 790 Bai, Quan, S. J. Mackwell, and D. L. Kohlstedt. 1991. “High-Temperature Creep of Olivine Single
791 Crystals 1. Mechanical Results for Buffered Samples.” *Journal of Geophysical Research, [Solid
792 Earth]* 96 (B2): 2441–63.
- 793 Bammann, D. J. 1989. “A Micro-Mechanically Motivated Model of Finite Deformation Plasticity.” In
794 *Advances in Plasticity 1989*, edited by Akhtar S. Khan and Masataka Tokuda, 283–86. Oxford:
795 Pergamon.
- 796 Bayley, C. J., W. A. M. Brekelmans, and M. G. D. Geers. 2006. “A Comparison of Dislocation Induced
797 Back Stress Formulations in Strain Gradient Crystal Plasticity.” *International Journal of Solids and
798 Structures* 43 (24): 7268–86.
- 799 Benjamin Britton, T., and Angus J. Wilkinson. 2012. “Stress Fields and Geometrically Necessary
800 Dislocation Density Distributions near the Head of a Blocked Slip Band.” *Acta Materialia* 60 (16):

- 801 5773–82.
- 802 Biberger, M., and J. C. Gibeling. 1995. “Analysis of Creep Transients in Pure Metals Following Stress
803 Changes.” *Acta Metallurgica et Materialia*. [https://doi.org/10.1016/0956-7151\(95\)00052-w](https://doi.org/10.1016/0956-7151(95)00052-w).
- 804 Bierson, C. J., and F. Nimmo. 2016. “A Test for Io’s Magma Ocean: Modeling Tidal Dissipation with a
805 Partially Molten Mantle.” *Journal of Geophysical Research: Planets*.
806 <https://doi.org/10.1002/2016je005005>.
- 807 Blum, W., and A. Finkel. 1982. “New Technique for Evaluating Long Range Internal Back Stresses.”
808 *Acta Metallurgica* 30 (8): 1705–15.
- 809 Blum, W., and E. Weckert. 1987. “On the Interpretation of the ‘Internal Stress’ Determined from Dip
810 Tests during Creep of Al-5at.%Mg.” *Materials Science and Engineering*.
811 [https://doi.org/10.1016/0025-5416\(87\)90449-6](https://doi.org/10.1016/0025-5416(87)90449-6).
- 812 Britton, T. B., J. Jiang, Y. Guo, A. Vilalta-Clemente, D. Wallis, L. N. Hansen, A. Winkelmann, and A. J.
813 Wilkinson. 2016. “Tutorial: Crystal Orientations and EBSD — Or Which Way Is Up?” *Materials*
814 *Characterization* 117: 113–26.
- 815 Britton, T. B., and A. J. Wilkinson. 2011. “Measurement of Residual Elastic Strain and Lattice Rotations
816 with High Resolution Electron Backscatter Diffraction.” *Ultramicroscopy* 111 (8): 1395–1404.
- 817 ———. 2012. “High Resolution Electron Backscatter Diffraction Measurements of Elastic Strain
818 Variations in the Presence of Larger Lattice Rotations.” *Ultramicroscopy* 114: 82–95.
- 819 Čadek, Josef. 1987. “The Back Stress Concept in Power Law Creep of Metals: A Review.” *International*
820 *Journal of Green Nanotechnology: Materials Science and Engineering* 94 (October): 79–92.
- 821 Caillard, D., and J. L. Martin. 2003. *Thermally Activated Mechanisms in Crystal Plasticity*. Elsevier.
- 822 Cao, Ri, Lars N. Hansen, Christopher A. Thom, and David Wallis. 2020. “An Apparatus for Measuring
823 Nonlinear Viscoelasticity of Minerals at High Temperature.” <https://doi.org/10.31223/X59W2X>.
- 824 Carcione, J. M., F. Poletto, B. Farina, and A. Craglietto. 2014. “Simulation of Seismic Waves at the
825 Earth’s Crust (brittle-Ductile Transition) Based on the Burgers Model.” *Solid Earth* 5 (2): 1001.
- 826 Caswell, Tess E., Reid F. Cooper, and David L. Goldsby. 2015. “The Constant-Hardness Creep
827 Compliance of Polycrystalline Ice.” *Geophysical Research Letters* 42 (15): 6261–68.
- 828 Chopra, Prame N. 1997. “High-Temperature Transient Creep in Olivine Rocks.” *Tectonophysics*.
829 [https://doi.org/10.1016/s0040-1951\(97\)00134-0](https://doi.org/10.1016/s0040-1951(97)00134-0).
- 830 Cooper, Reid F., Donald S. Stone, and Thawatchai Plookphol. 2016. “Load Relaxation of Olivine Single
831 Crystals.” *Journal of Geophysical Research: Solid Earth*. <https://doi.org/10.1002/2016jb013425>.
- 832 Demouchy, Sylvie, Andréa Tommasi, Tiziana Boffa Ballaran, and Patrick Cordier. 2013. “Low Strength
833 of Earth’s Uppermost Mantle Inferred from Tri-Axial Deformation Experiments on Dry Olivine
834 Crystals.” *Physics of the Earth and Planetary Interiors* 220 (July): 37–49.
- 835 Durham, W. B., and C. Goetze. 1977. “Plastic Flow of Oriented Single Crystals of Olivine: 1. Mechanical
836 Data.” *Journal of Geophysical Research* 82 (36): 5737–53.
- 837 Durham, W. B., C. Goetze, and B. Blake. 1977. “Plastic Flow of Oriented Single Crystals of Olivine: 2.
838 Observations and Interpretations of the Dislocation Structures.” *Journal of Geophysical Research*.
839 <https://doi.org/10.1029/jb082i036p05755>.
- 840 Duval, P., M. F. Ashby, and I. Anderman. 1983. “Rate-Controlling Processes in the Creep of
841 Polycrystalline Ice.” *The Journal of Physical Chemistry* 87 (21): 4066–74.
- 842 Evans, R. W., W. J. F. Roach, and B. Wilshire. 1985. “Creep of Aluminium Following Stress
843 Reductions.” *Scripta Metallurgica* 19 (8): 999–1003.
- 844 Faul, Ulrich H., and Ian Jackson. 2005. “The Seismological Signature of Temperature and Grain Size
845 Variations in the Upper Mantle.” *Earth and Planetary Science Letters* 234 (1): 119–34.
- 846 Field, Edward H., Glenn P. Biasi, Peter Bird, Timothy E. Dawson, Karen R. Felzer, David D. Jackson,
847 Kaj M. Johnson, et al. 2015. “Long-Term Time-Dependent Probabilities for the Third Uniform
848 California Earthquake Rupture Forecast (UCERF3).” *Bulletin of the Seismological Society of*

- 849 *America* 105 (2A): 511–43.
- 850 Field, Edward H., Thomas H. Jordan, Morgan T. Page, Kevin R. Milner, Bruce E. Shaw, Timothy E.
851 Dawson, Glenn P. Biasi, et al. 2017. “A Synoptic View of the Third Uniform California Earthquake
852 Rupture Forecast (UCERF3).” *Seismological Research Letters* 88 (5): 1259–67.
- 853 Freed, Andrew M. 2005. “Earthquake Triggering by Static, Dynamic, and Postseismic Stress Transfer.”
854 *Annual Review of Earth and Planetary Sciences* 33 (1): 335–67.
- 855 Freed, Andrew M., Greg Hirth, and Mark D. Behn. 2012. “Using Short-Term Postseismic Displacements
856 to Infer the Ambient Deformation Conditions of the Upper Mantle.” *Journal of Geophysical
857 Research* 117 (B1). <https://doi.org/10.1029/2011JB008562>.
- 858 Frost, H. J., and M. F. Ashby. 1982. *Deformation Mechanism Maps: The Plasticity and Creep of Metals
859 and Ceramics*. Oxford, UK: Pergamon Press.
- 860 Garmestani, H., M. R. Vaghar, and E. W. Hart. 2001. “A Unified Model for Inelastic Deformation of
861 Polycrystalline Materials—application to Transient Behavior in Cyclic Loading and Relaxation.”
862 *International Journal of Plasticity* 17 (10): 1367–91.
- 863 Garofalo, and F. 1963. “An Empirical Relation Defining the Stress Dependence of Minimum Creep Rate
864 in Metals.” *Trans. AIME* 227: 351–56.
- 865 Gibbs, G. B. 1966. “Creep and Stress Relaxation Studies with Polycrystalline Magnesium.” *The
866 Philosophical Magazine: A Journal of Theoretical Experimental and Applied Physics* 13 (122): 317–
867 29.
- 868 Gibeling, J. C., and W. D. Nix. 1981. “Observations of Anelastic Backflow Following Stress Reductions
869 during Creep of Pure Metals.” *Acta Metallurgica* 29 (10): 1769–84.
- 870 Goetze, C., and D. L. Kohlstedt. 1973. “Laboratory Study of Dislocation Climb and Diffusion in
871 Olivine.” *Journal of Geophysical Research* 78 (26): 5961–71.
- 872 Gribb, Tye T., and Reid F. Cooper. 1998. “Low-Frequency Shear Attenuation in Polycrystalline Olivine:
873 Grain Boundary Diffusion and the Physical Significance of the Andrade Model for Viscoelastic
874 Rheology.” *Journal of Geophysical Research: Solid Earth*. <https://doi.org/10.1029/98jb02786>.
- 875 Gupta, I., and J. C. M. Li. 1970. “Stress Relaxation, Internal Stress and Work Hardening in LiF and NaCl
876 Crystals.” *International Journal of Green Nanotechnology: Materials Science and Engineering* 6
877 (1): 20–26.
- 878 Hansen, Lars N., Kathryn M. Kumamoto, Christopher A. Thom, David Wallis, William B. Durham,
879 David L. Goldsby, Thomas Breithaupt, Cameron D. Meyers, and David L. Kohlstedt. 2019. “Low-
880 temperature Plasticity in Olivine: Grain Size, Strain Hardening, and the Strength of the Lithosphere.”
881 *Journal of Geophysical Research: Solid Earth*. <https://doi.org/10.1029/2018jb016736>.
- 882 Hanson, David R., and Hartmut A. Spetzler. 1994. “Transient Creep in Natural and Synthetic, Iron-
883 Bearing Olivine Single Crystals: Mechanical Results and Dislocation Microstructures.”
884 *Tectonophysics*. [https://doi.org/10.1016/0040-1951\(94\)90191-0](https://doi.org/10.1016/0040-1951(94)90191-0).
- 885 Hart, E. W. 1970. “A Phenomenological Theory for Plastic Deformation of Polycrystalline Metals.” *Acta
886 Metallurgica* 18 (6): 599–610.
- 887 ———. 1976. “Constitutive Relations for the Nonelastic Deformation of Metals.” *Journal of Engineering
888 Materials and Technology* 98 (3): 193–202.
- 889 Hetland, E. A., and B. H. Hager. 2005. “Postseismic and Interseismic Displacements near a Strike-Slip
890 Fault: A Two-Dimensional Theory for General Linear Viscoelastic Rheologies.” *Journal of
891 Geophysical Research, [Solid Earth]* 110 (B10).
892 <https://agupubs.onlinelibrary.wiley.com/doi/abs/10.1029/2005JB003689>.
- 893 Hirth, Greg, and David Kohlstedt. 2003. “Rheology of the Upper Mantle and the Mantle Wedge: A View
894 from the Experimentalists.” In *Geophysical Monograph Series*, edited by John Eiler, 138:83–105.
895 Washington, D. C.: American Geophysical Union.
- 896 Hunter, J., and A. B. Watts. 2016. “Gravity Anomalies, Flexure and Mantle Rheology Seaward of

- 897 Circum-Pacific Trenches.” *Geophysical Journal International* 207 (1): 288–316.
- 898 Jackson, Ian, John D. Fitz Gerald, Ulrich H. Faul, and Ben H. Tan. 2002. “Grain-Size-Sensitive Seismic
899 Wave Attenuation in Polycrystalline Olivine.” *Journal of Geophysical Research: Solid Earth*.
900 <https://doi.org/10.1029/2001jb001225>.
- 901 Jackson, I., U. H. Faul, and R. Skelton. 2014. “Elastically Accommodated Grain-Boundary Sliding: New
902 Insights from Experiment and Modeling.” *Physics of the Earth and Planetary Interiors* 228: 203–10.
- 903 Jain, Chhavi, Jun Korenaga, and Shun-Ichiro Karato. 2017. “On the Yield Strength of Oceanic
904 Lithosphere.” *Geophysical Research Letters* 44 (19): 9716–22.
- 905 Karato, Shun-Ichiro. 2012. “On the Origin of the Asthenosphere.” *Earth and Planetary Science Letters*
906 321: 95–103.
- 907 Karato, Shun-Ichiro, Mervyn S. Paterson, and John D. FitzGerald. 1986. “Rheology of Synthetic Olivine
908 Aggregates: Influence of Grain Size and Water.” *Journal of Geophysical Research* 91 (B8): 8151–
909 76.
- 910 Karato, Shun-Ichiro, David C. Rubie, and Hong Yan. 1993. “Dislocation Recovery in Olivine under Deep
911 Upper Mantle Conditions: Implications for Creep and Diffusion.” *Journal of Geophysical Research*
912 98 (B6): 9761–68.
- 913 Karato, S., and H. A. Spetzler. 1990. “Defect Microdynamics in Minerals and Solid-State Mechanisms of
914 Seismic Wave Attenuation and Velocity Dispersion in the Mantle.” *Reviews of Geophysics*.
915 <https://doi.org/10.1029/rg028i004p00399>.
- 916 Kassner, Michael E. 2015. *Fundamentals of Creep in Metals and Alloys*. Butterworth-Heinemann.
- 917 Kocks, U. F., A. S. Argon, and M. F. Ashby. 1975. “Thermodynamics and Kinetics of Slip.” *Progress in*
918 *Materials Science* 19.
- 919 Korhonen, M. A., S-P Hannula, and Che-Yu Li. 1987. “State Variable Theories Based on Hart’s
920 Formulation.” In *Unified Constitutive Equations for Creep and Plasticity*, 89–137. Springer.
- 921 Krausz, A. S. 1968. “A Rate Theory of Dislocation Mobility.” *Acta Metallurgica* 16 (7): 897–902.
- 922 Kumamoto, Kathryn M., Christopher A. Thom, David Wallis, Lars N. Hansen, David E. J. Armstrong,
923 Jessica M. Warren, David L. Goldsby, and Angus J. Wilkinson. 2017. “Size Effects Resolve
924 Discrepancies in 40 Years of Work on Low-Temperature Plasticity in Olivine.” *Science Advances* 3
925 (9): e1701338.
- 926 Long, Hongbo, Donald J. Weidner, Li Li, Jihua Chen, and Liping Wang. 2011. “Deformation of Olivine
927 at Subduction Zone Conditions Determined from in Situ Measurements with Synchrotron
928 Radiation.” *Physics of the Earth and Planetary Interiors* 186 (1–2): 23–35.
- 929 Masuti, Sagar, Sylvain D. Barbot, Shun-Ichiro Karato, Lujia Feng, and Paramesh Banerjee. 2016.
930 “Upper-Mantle Water Stratification Inferred from Observations of the 2012 Indian Ocean
931 Earthquake.” *Nature* 538 (7625): 373–77.
- 932 Masuti, Sagar, Shun-Ichiro Karato, Jennifer Girard, and Sylvain D. Barbot. 2019. “Anisotropic High-
933 Temperature Creep in Hydrous Olivine Single Crystals and Its Geodynamic Implications.” *Physics*
934 *of the Earth and Planetary Interiors* 290 (May): 1–9.
- 935 Mecking, H., and U. F. Kocks. 1981. “Kinetics of Flow and Strain-Hardening.” *Acta Metallurgica*.
936 [https://doi.org/10.1016/0001-6160\(81\)90112-7](https://doi.org/10.1016/0001-6160(81)90112-7).
- 937 Menezes, R. A., and W. D. Nix. 1971. “Average Internal Stresses in LiF Single Crystals during High
938 Temperature Creep.” *Acta Metallurgica* 19 (7): 645–49.
- 939 Meyssonier, J., and A. Goubert. 1994. “Transient Creep of Polycrystalline Ice under Uniaxial
940 Compression: An Assessment of Internal State Variable Models.” *Annals of Glaciology*.
941 <https://doi.org/10.1017/s0260305500010983>.
- 942 Milička, Karel, Zuzanka Trojanová, and Pavel Lukáč. 2007. “Internal Stresses during Creep of
943 Magnesium Alloys at 523 K.” *Materials Science and Engineering: A* 462 (1-2): 215–19.
- 944 Mughrabi, H. 1980. “Strength of Metals and Alloys.” In *Proc. Intern. Conf. Metals and Alloys*, Ed. by P.

- 945 Haasen, V. Gerold and G. Kostorz, Pergamon, Oxford, 1615.
- 946 Müller, W., M. Biberger, and W. Blum. 1992. “Subgrain-Boundary Migration during Creep of Lif III.
- 947 Stress Reduction Experiments.” *Philosophical Magazine A*.
- 948 <https://doi.org/10.1080/01418619208201586>.
- 949 Nimmo, F., and U. H. Faul. 2013. “Dissipation at Tidal and Seismic Frequencies in a Melt-Free,
- 950 Anhydrous Mars.” *Journal of Geophysical Research: Planets* 118 (12): 2558–69.
- 951 Nimmo, F., U. H. Faul, and E. J. Garnero. 2012. “Dissipation at Tidal and Seismic Frequencies in a Melt-
- 952 Free Moon.” *Journal of Geophysical Research: Planets* 117 (E9).
- 953 <https://agupubs.onlinelibrary.wiley.com/doi/abs/10.1029/2012JE004160>.
- 954 Nix, W. D., and B. Ilshner. 1979. “Mechanisms Controlling Creep of Single Phase Metals and Alloys.”
- 955 In *Strength of Metals and Alloys*, edited by P. Haasen, V. Gerold, and G. Kostorz, 1503–30.
- 956 Pergamon.
- 957 Poirier, J. P. 1977. “Microscopic Creep Models and the Interpretation of Stress-Drop Tests during Creep.”
- 958 *Acta Metallurgica*. [https://doi.org/10.1016/0001-6160\(77\)90178-x](https://doi.org/10.1016/0001-6160(77)90178-x).
- 959 Pollitz, Fred F. 2005. “Transient Rheology of the Upper Mantle beneath Central Alaska Inferred from the
- 960 Crustal Velocity Field Following the 2002 Denali Earthquake.” *Journal of Geophysical Research*
- 961 110 (B8). <https://doi.org/10.1029/2005jb003672>.
- 962 Pollitz, Fred F., Roland Bürgmann, and Paramesh Banerjee. 2006. “Post-Seismic Relaxation Following
- 963 the Great 2004 Sumatra-Andaman Earthquake on a Compressible Self-Gravitating Earth.”
- 964 *Geophysical Journal International* 167 (1): 397–420.
- 965 Post, Robert L., Jr. 1977. “High-Temperature Creep of Mt. Burnet Dunite.” *Tectonophysics* 42 (2-4): 75–
- 966 110.
- 967 Qiu, Qiang, James D. P. Moore, Sylvain Barbot, Lujia Feng, and Emma M. Hill. 2018. “Transient
- 968 Rheology of the Sumatran Mantle Wedge Revealed by a Decade of Great Earthquakes.” *Nature*
- 969 *Communications* 9 (1): 995.
- 970 Rumpker, Georg, and Detlef Wolff. 1996. “Viscoelastic Relaxation of a Burgers Half-Space: Implications
- 971 for the Interpretation of the Fennoscandian Uplift.” *Geophysical Journal International*.
- 972 <https://doi.org/10.1111/j.1365-246x.1996.tb07036.x>.
- 973 Smith, B. K., and F. O. Carpenter. 1987. “Transient Creep in Orthosilicates.” *Physics of the Earth and*
- 974 *Planetary Interiors*. [https://doi.org/10.1016/0031-9201\(87\)90033-1](https://doi.org/10.1016/0031-9201(87)90033-1).
- 975 Stone, D. S. 1991. “Scaling Laws in Dislocation Creep.” *Acta Metallurgica et Materialia* 39 (4): 599–
- 976 608.
- 977 Stone, D. S., T. Ploekphol, and R. F. Cooper. 2004. “Similarity and Scaling in Creep and Load Relaxation
- 978 of Single-Crystal Halite (NaCl).” *Journal of Geophysical Research, [Solid Earth]* 109 (B12).
- 979 <https://agupubs.onlinelibrary.wiley.com/doi/abs/10.1029/2004JB003064>.
- 980 Sundberg, Marshall, and Reid F. Cooper. 2010. “A Composite Viscoelastic Model for Incorporating
- 981 Grain Boundary Sliding and Transient Diffusion Creep; Correlating Creep and Attenuation
- 982 Responses for Materials with a Fine Grain Size.” *Philosophical Magazine* 90 (20): 2817–40.
- 983 Suzuki, Taira, Shin Takeuchi, and Hideo Yoshinaga. 2013. *Dislocation Dynamics and Plasticity*. Springer
- 984 Science & Business Media.
- 985 Takeuchi, S., and A. S. Argon. 1976. “Steady-State Creep of Single-Phase Crystalline Matter at High
- 986 Temperature.” *Journal of Materials Science* 11 (8): 1542–66.
- 987 Taylor, Geoffrey Ingram. 1934. “The Mechanism of Plastic Deformation of Crystals. Part I.—
- 988 Theoretical.” *Proceedings of the Royal Society of London. Series A, Containing Papers of a*
- 989 *Mathematical and Physical Character* 145 (855): 362–87.
- 990 Thieme, M., S. Demouchy, D. Mainprice, F. Barou, and P. Cordier. 2018. “Stress Evolution and
- 991 Associated Microstructure during Transient Creep of Olivine at 1000–1200 °C.” *Physics of the Earth*
- 992 *and Planetary Interiors*. <https://doi.org/10.1016/j.pepi.2018.03.002>.

- 993 Toriumi, Mitsuhiro. 1982. "Grain Boundary Migration in Olivine at Atmospheric Pressure." *Physics of*
994 *the Earth and Planetary Interiors* 30 (1): 26–35.
- 995 Toriumi, Mitsuhiro, and Shun-Ichiro Karato. 1978. "Experimental Studies on the Recovery Process of
996 Deformed Olivines and the Mechanical State of the Upper Mantle." *Tectonophysics* 49 (1): 79–95.
- 997 Wallis, David, Lars N. Hansen, T. Ben Britton, and Angus J. Wilkinson. 2016. "Geometrically Necessary
998 Dislocation Densities in Olivine Obtained Using High-Angular Resolution Electron Backscatter
999 Diffraction." *Ultramicroscopy* 168 (September): 34–45.
- 1000 ———. 2017. "Dislocation Interactions in Olivine Revealed by HR-EBSD." *Journal of Geophysical*
1001 *Research, [Solid Earth]* 122 (10): 7659–78.
- 1002 Wallis, David, Lars N. Hansen, Kathryn M. Kumamoto, Christopher A. Thom, Oliver Plümper, Markus
1003 Ohl, William B. Durham, et al. 2020. "Dislocation Interactions during Low-Temperature Plasticity
1004 of Olivine and Their Impact on the Evolution of Lithospheric Strength." *Earth and Planetary*
1005 *Science Letters* 543 (August): 116349.
- 1006 Wallis, David, Lars N. Hansen, Angus J. Wilkinson, and Ricardo A. Lebensohn. 2020. "Dislocation
1007 Interactions in Olivine Control Postseismic Creep of the Upper Mantle." *arXiv [cond-Mat.mtrl-Sci]*.
1008 arXiv. <http://arxiv.org/abs/2006.05195>.
- 1009 Wallis, D., L. N. Hansen, T. B. Britton, and A. J. Wilkinson. 2019. "High-Angular Resolution Electron
1010 Backscatter Diffraction as a New Tool for Mapping Lattice Distortion in Geological Minerals."
1011 *Journal of Geophysical Research: Solid Earth*. <https://doi.org/10.1029/2019jb017867>.
- 1012 Wang, Lin, Stephan Blaha, Zsanett Pintér, Robert Farla, Takaaki Kawazoe, Nobuyoshi Miyajima,
1013 Katsuyoshi Michibayashi, and Tomoo Katsura. 2016. "Temperature Dependence of [100](010) and
1014 [001](010) Dislocation Mobility in Natural Olivine." *Earth and Planetary Science Letters* 441
1015 (May): 81–90.
- 1016 Wang, Zichao, Shun-Ichiro Karato, and Kiyoshi Fujino. 1993. "High Temperature Creep of Single
1017 Crystal Strontium Titanate (SrTiO₃): A Contribution to Creep Systematics in Perovskites." *Physics*
1018 *of the Earth and Planetary Interiors* 79 (3): 299–312.
- 1019 ———. 1996. "High Temperature Creep of Single Crystal Gadolinium Gallium Garnet." *Physics and*
1020 *Chemistry of Minerals*. <https://doi.org/10.1007/bf00202301>.
- 1021 Weertman, J. 1957. "Steady-State Creep of Crystals." *Journal of Applied Physics* 28 (10): 1185–89.
- 1022 Wilkinson, Angus J., Graham Meaden, and David J. Dingley. 2006. "High-Resolution Elastic Strain
1023 Measurement from Electron Backscatter Diffraction Patterns: New Levels of Sensitivity."
1024 *Ultramicroscopy* 106 (4-5): 307–13.
- 1025 Wilson, J. F., and N. K. Wilson. 1966. "Kinetics of Stress Relaxation in Metals." *Transactions of the*
1026 *Society of Rheology* 10 (1): 399–418.
- 1027 Wu, X. J., and A. S. Krausz. 1994. "A Kinetics Formulation for Low-Temperature Plasticity." *Journal of*
1028 *Materials Engineering and Performance* 3 (1): 169–77.
- 1029 Yuen, David A., Roberto C. A. Sabadini, Paolo Gasperini, and Enzo Boschi. 1986. "On Transient
1030 Rheology and Glacial Isostasy." *Journal of Geophysical Research, Geophys. Monogr*, 91 (B11):
1031 11420.
- 1032 Zhong, Shijie, and A. B. Watts. 2013. "Lithospheric Deformation Induced by Loading of the Hawaiian
1033 Islands and Its Implications for Mantle Rheology." *Journal of Geophysical Research, [Solid Earth]*
1034 118 (11): 2013JB010408.

1035

Figure 1.

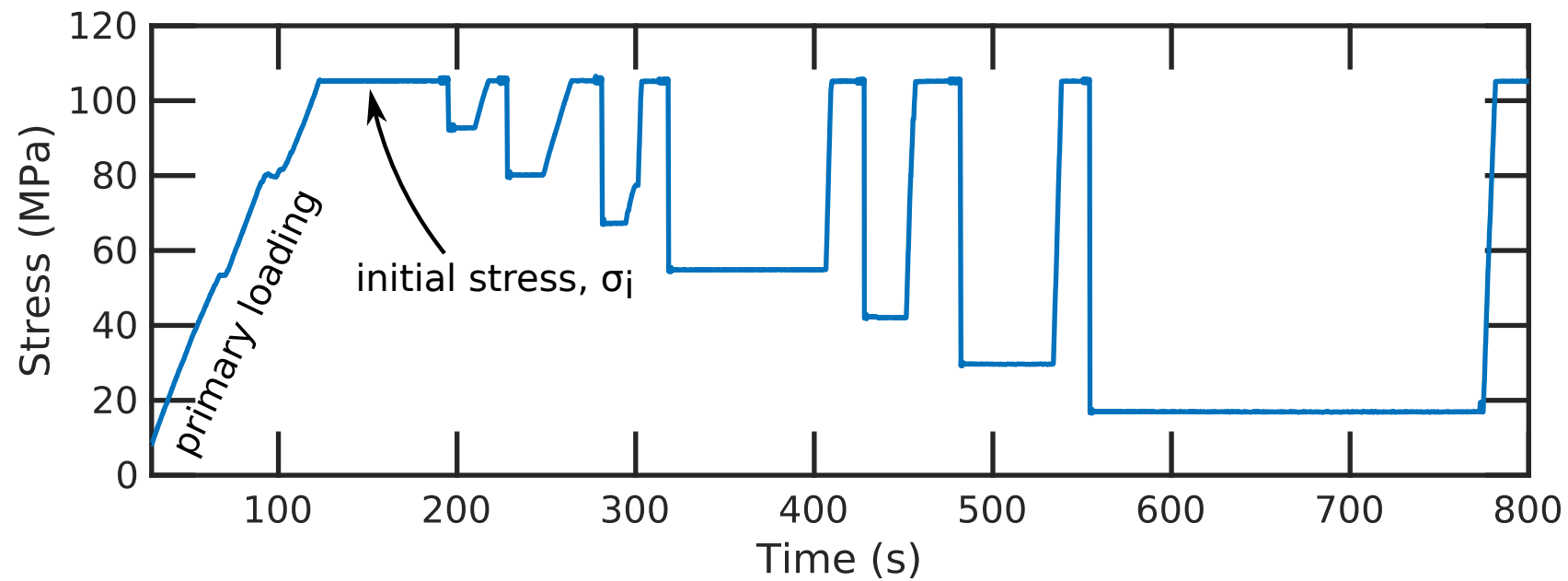
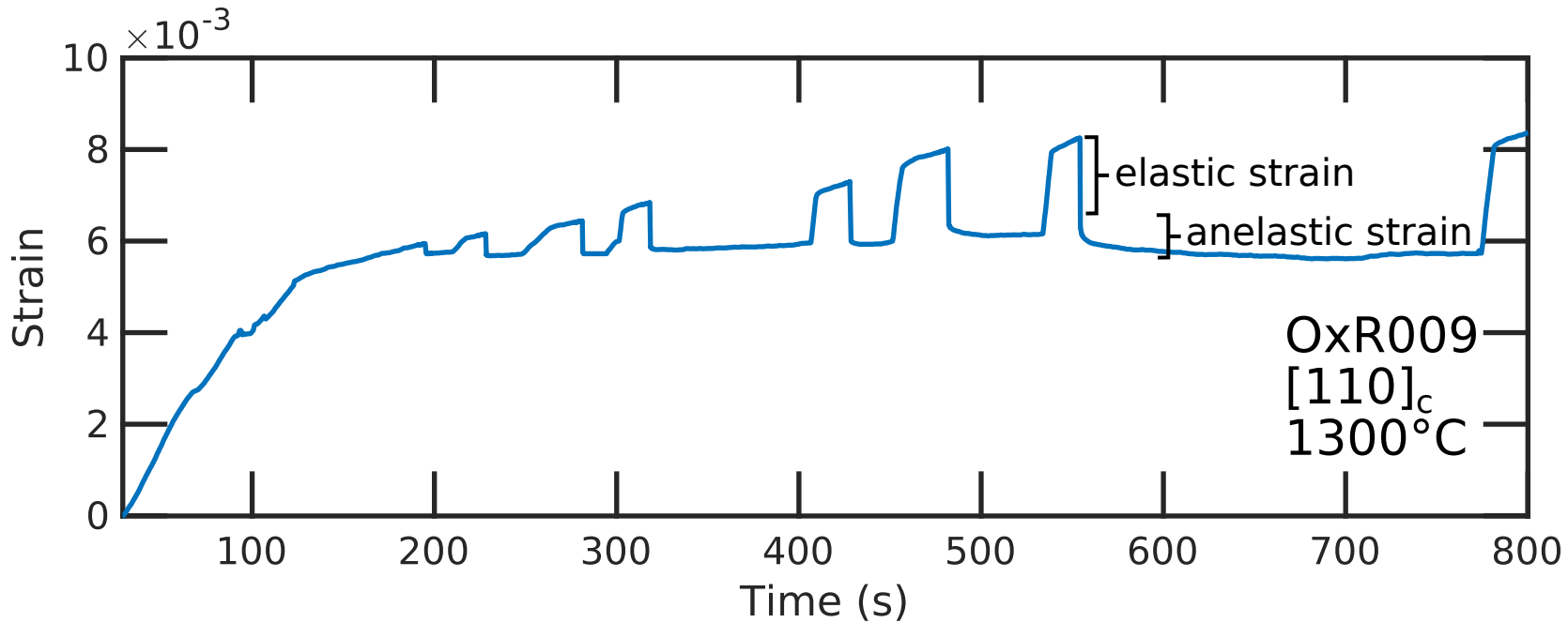


Figure 2.

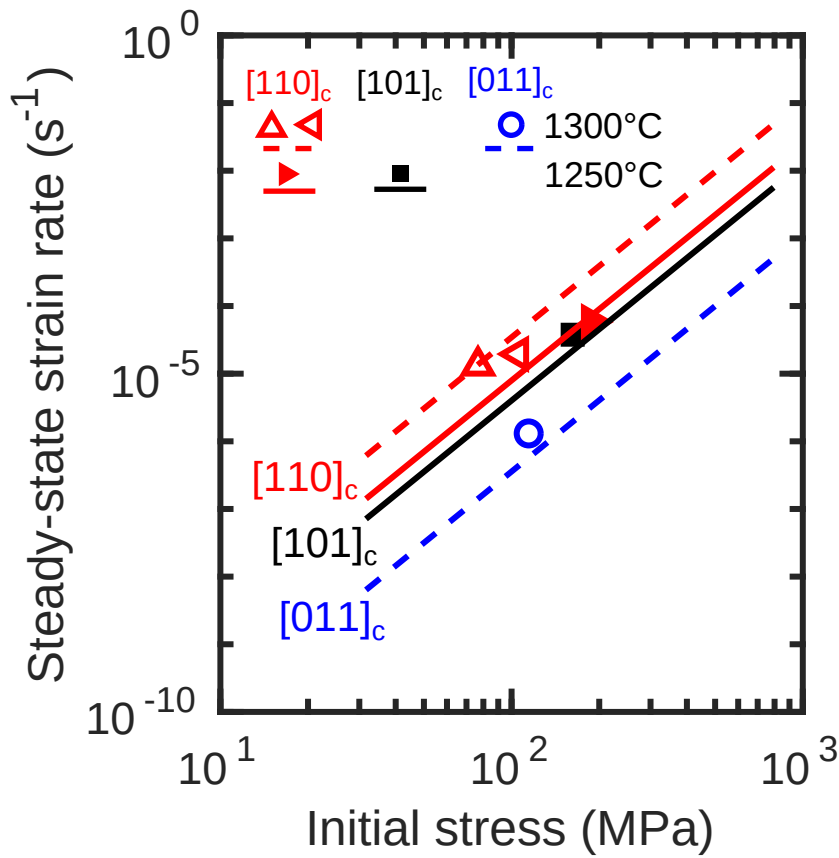
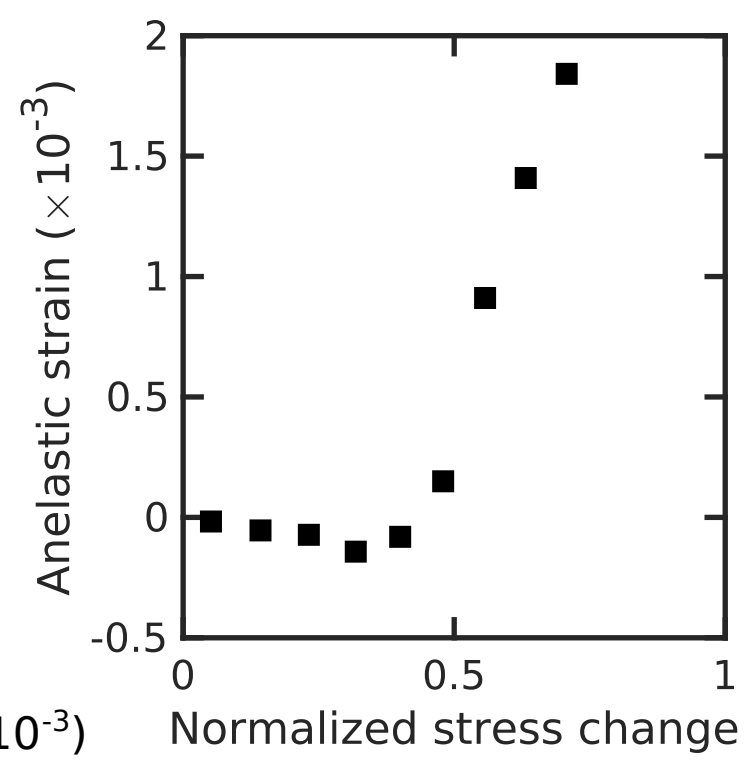
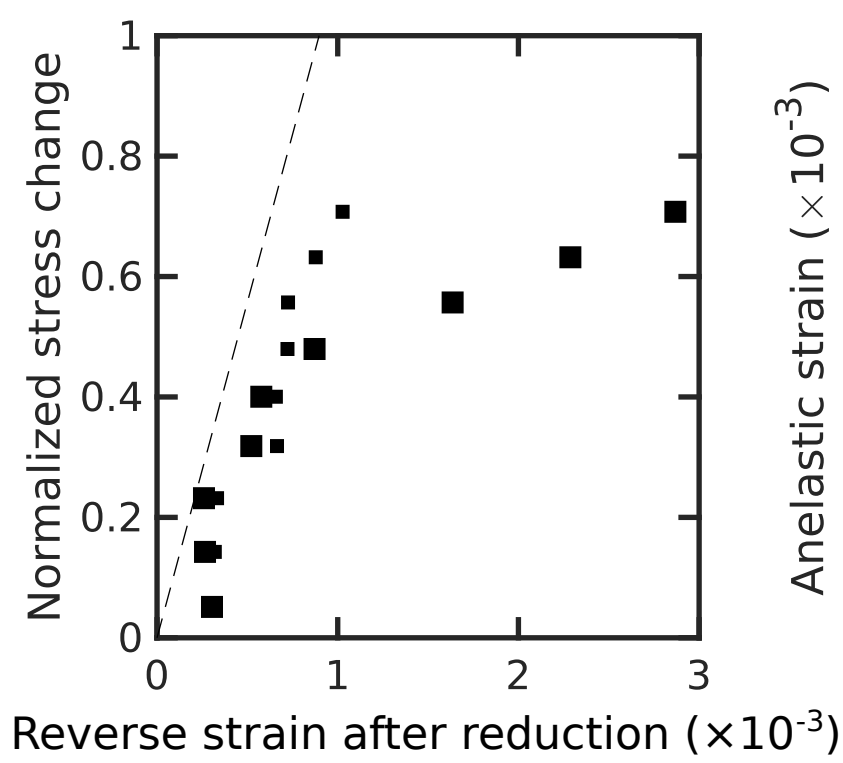
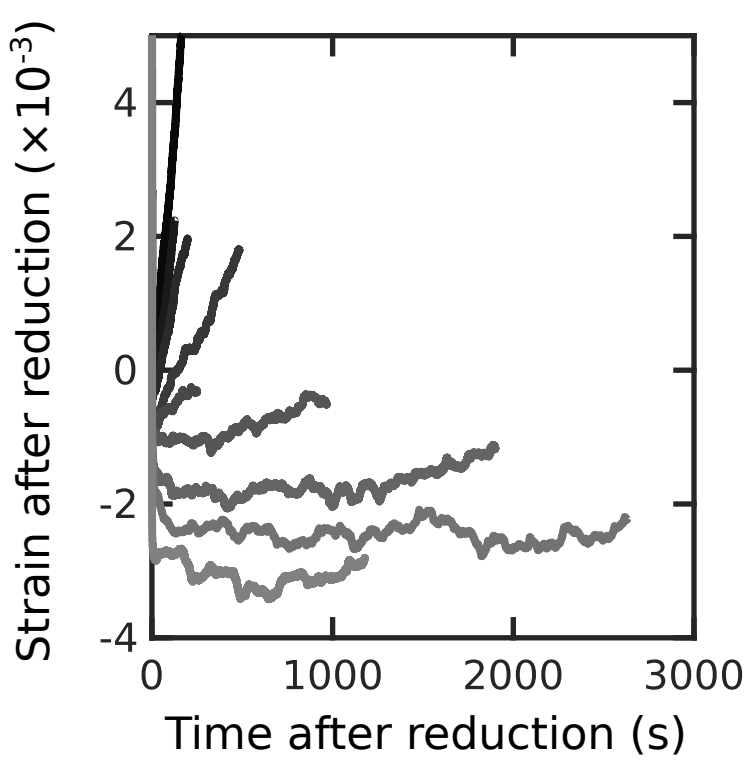
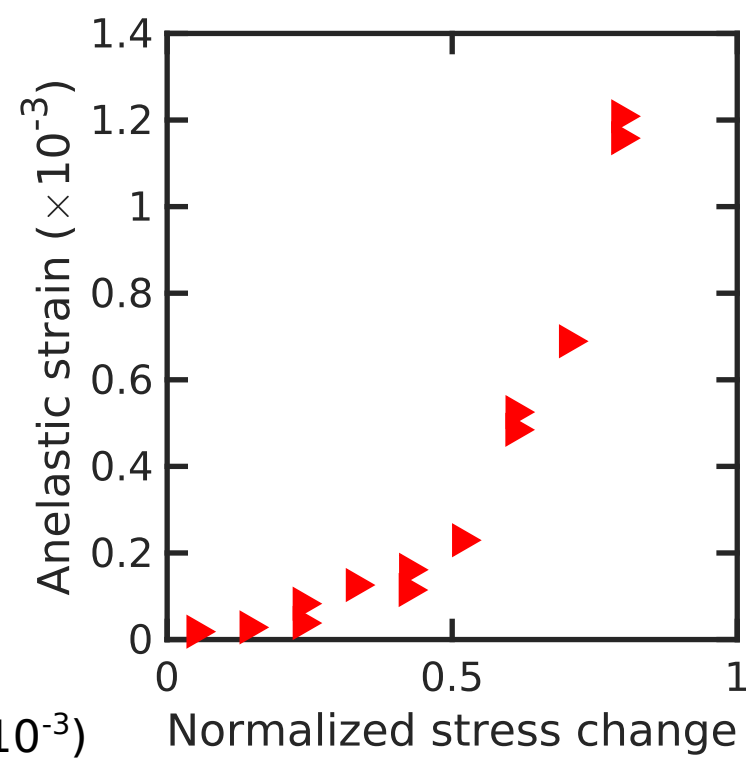
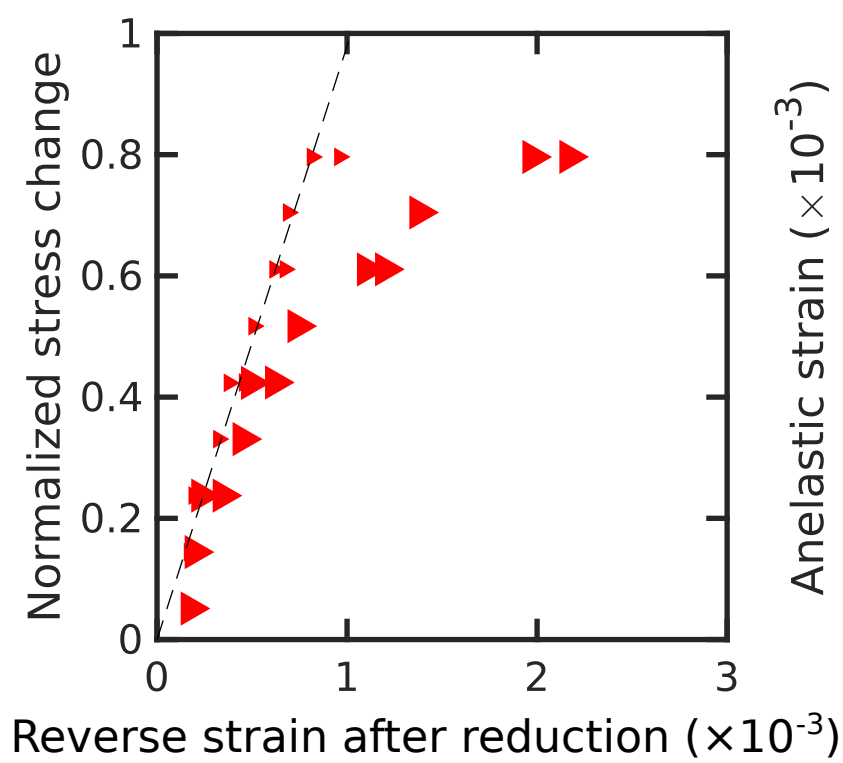
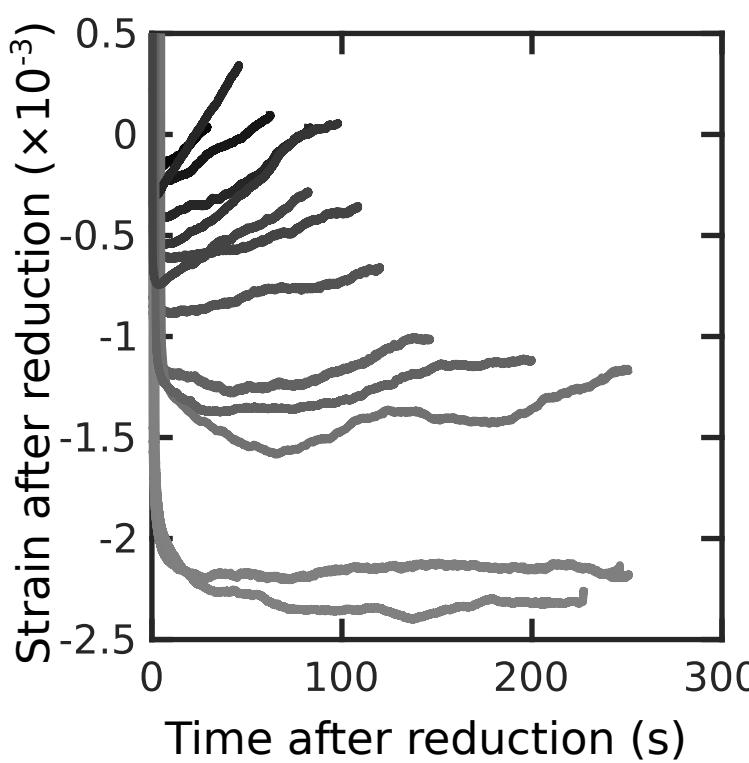


Figure 3.

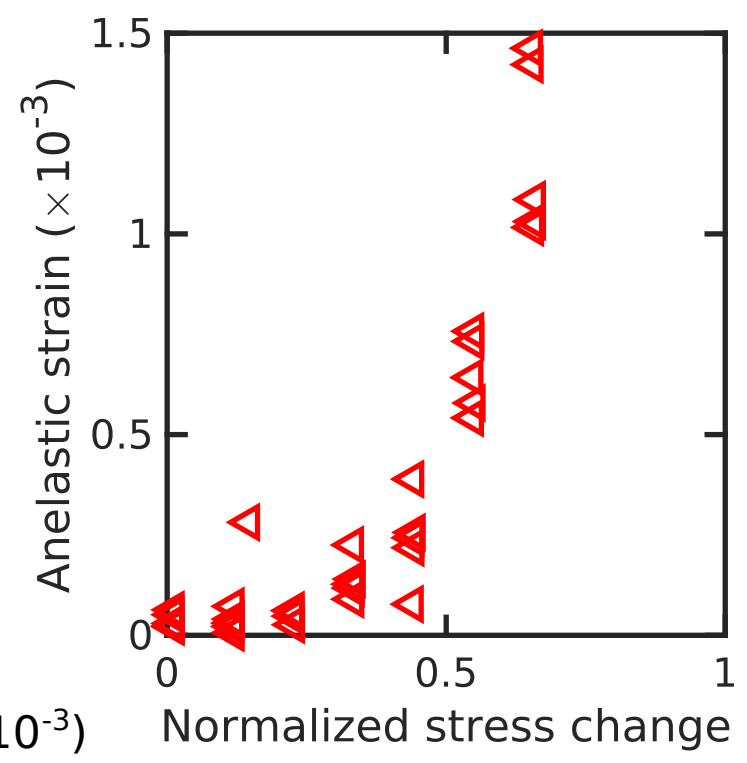
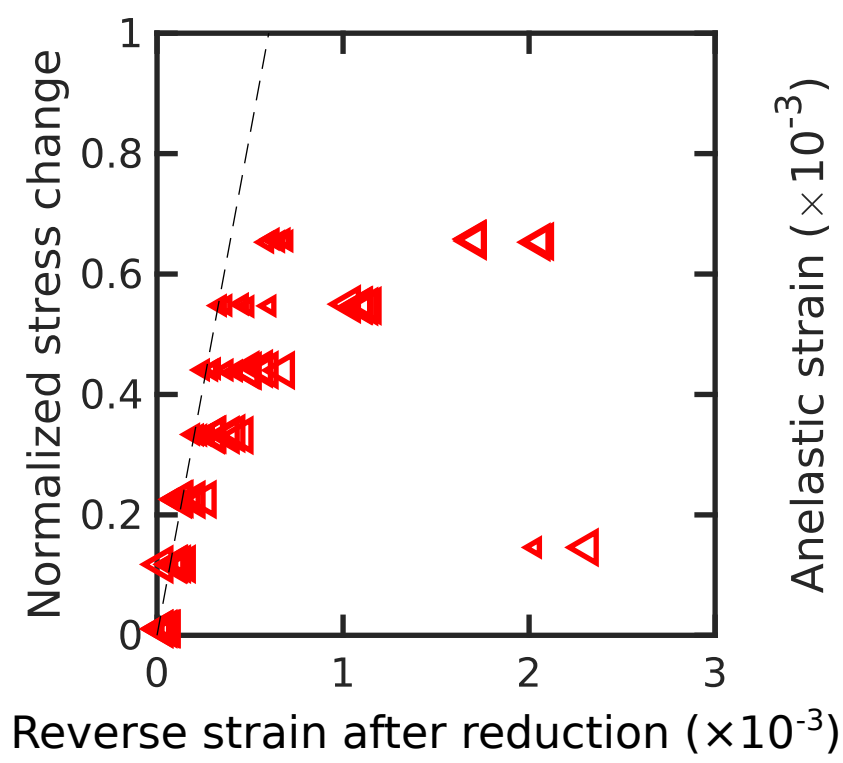
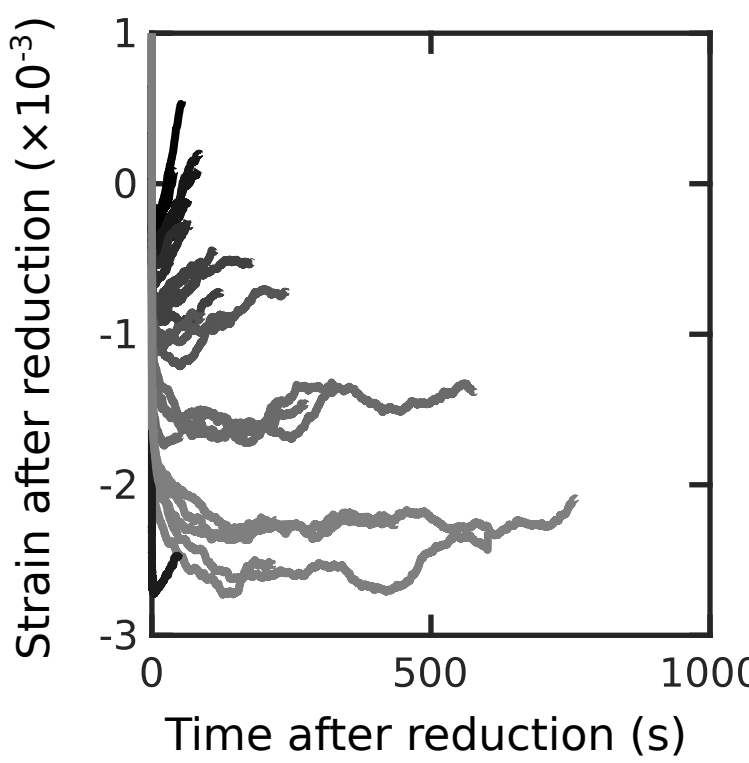
OxR0002
[101]_c
T = 1250°C
σ_i = 162 MPa



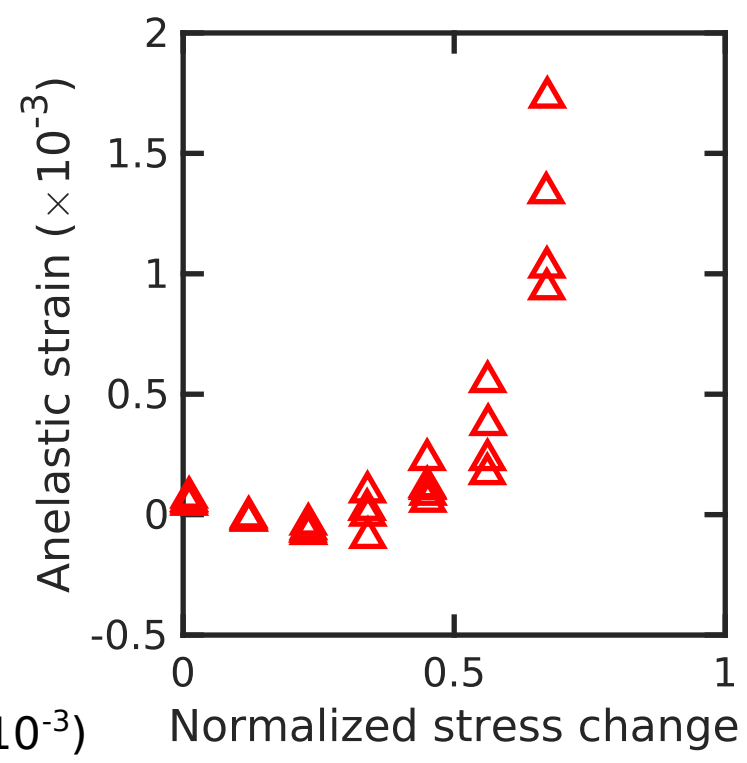
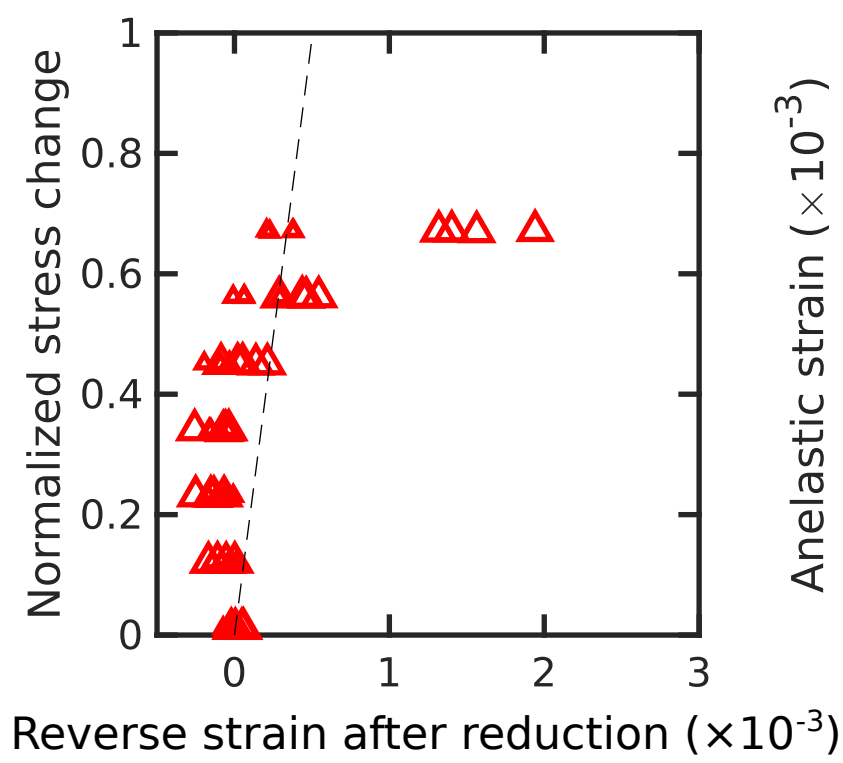
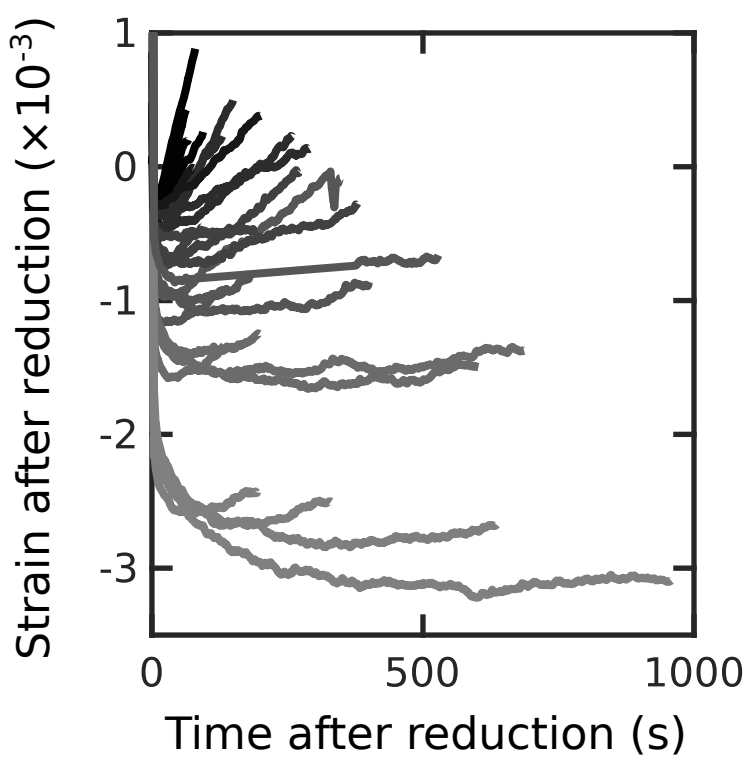
OxR0007
[110]_c
T = 1250°C
σ_i = 189 MPa



OxR0009
[110]_c
T = 1300°C
σ_i = 105 MPa



OxR0009b
[110]_c
T = 1300°C
σ_i = 77 MPa



OxR0010
[011]_c
T = 1300°C
σ_i = 116 MPa

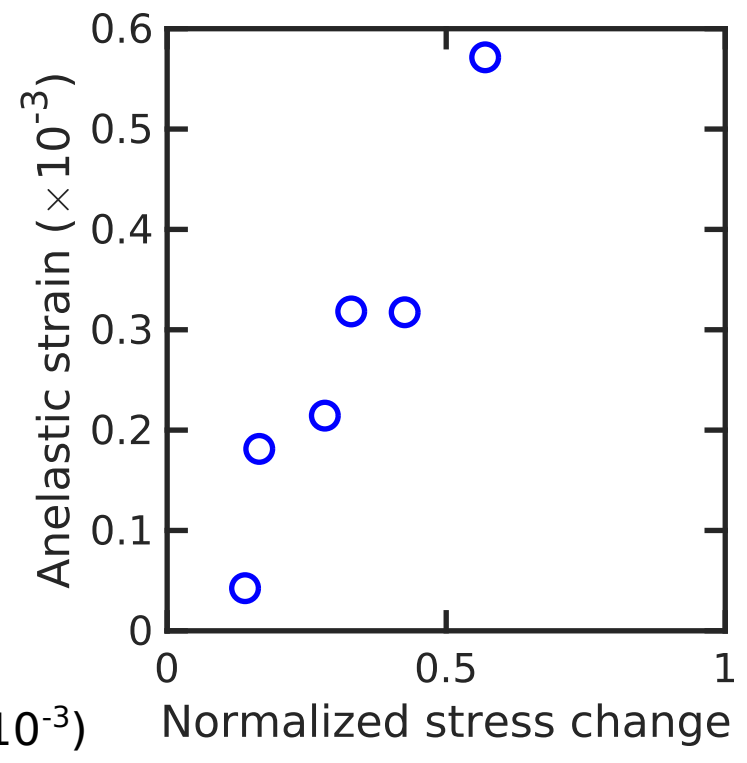
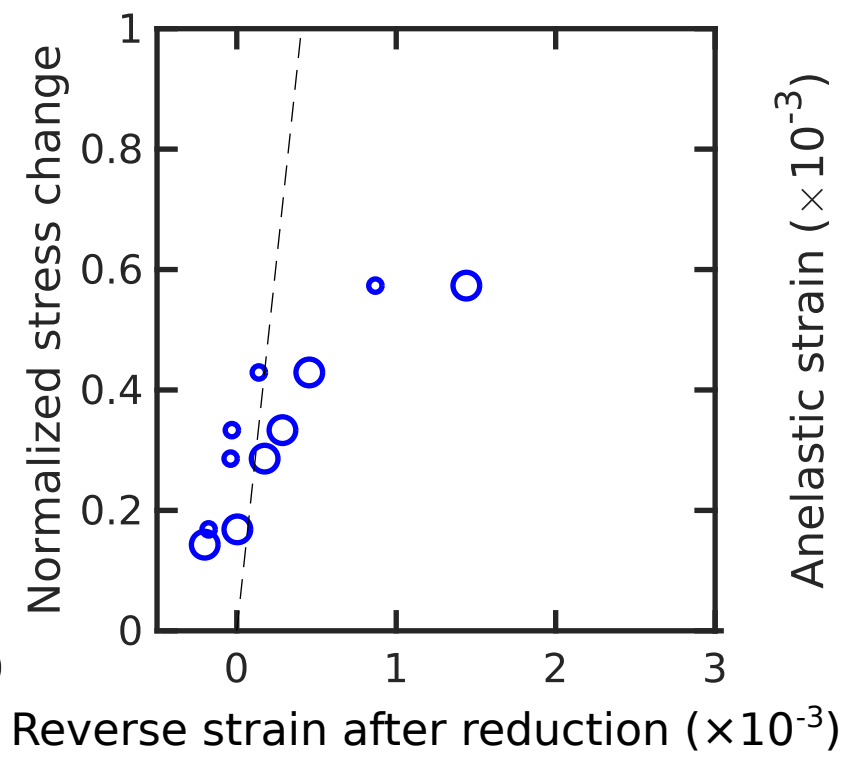
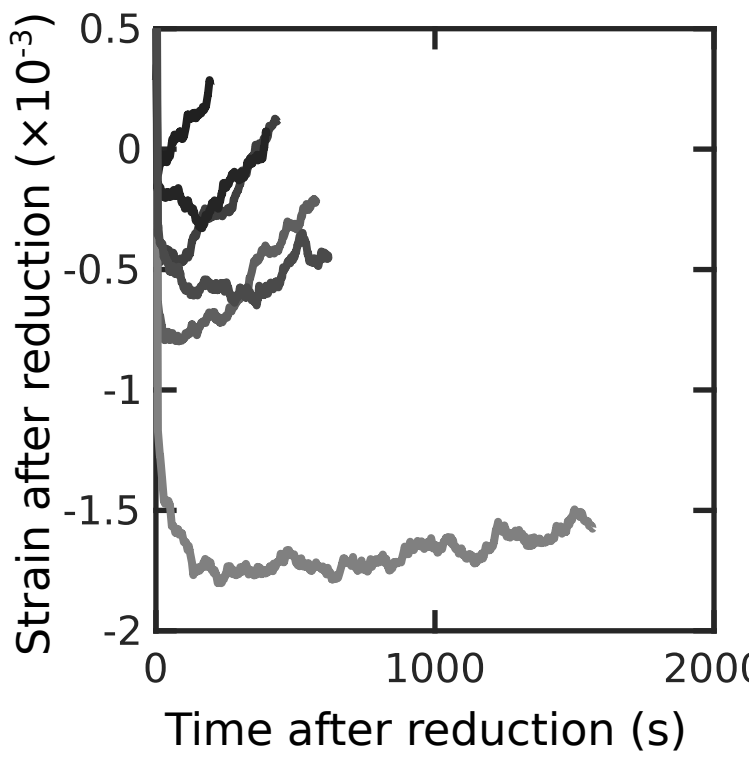


Figure 4.

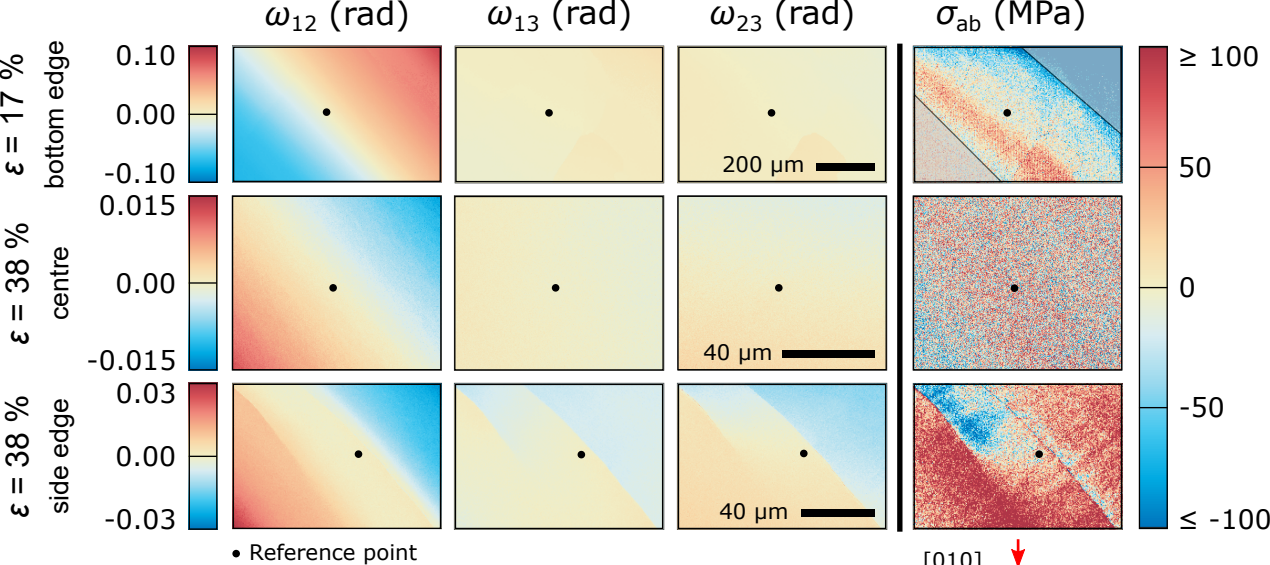


Figure 5.

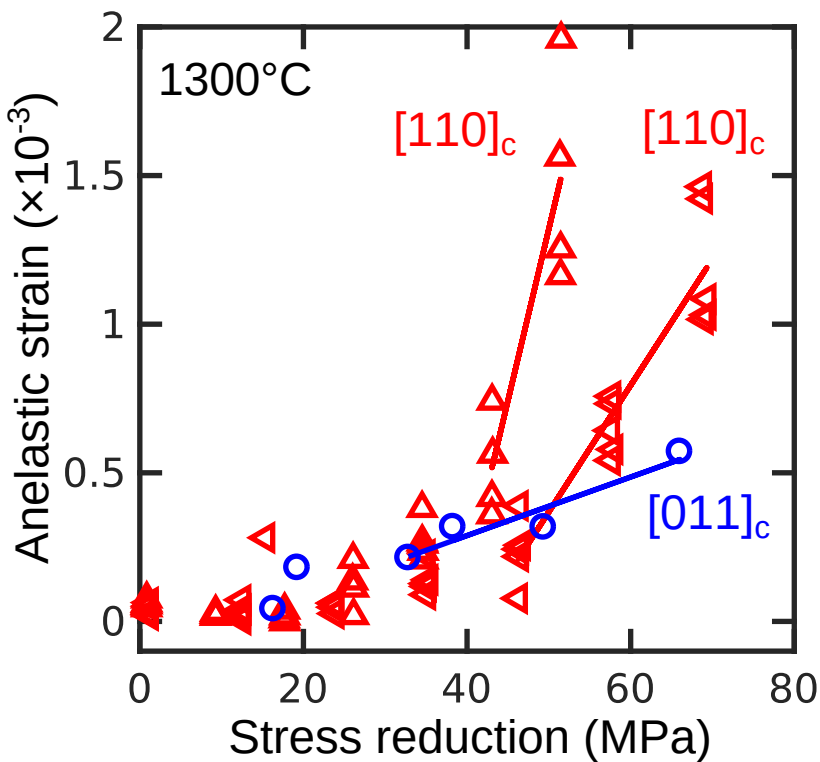
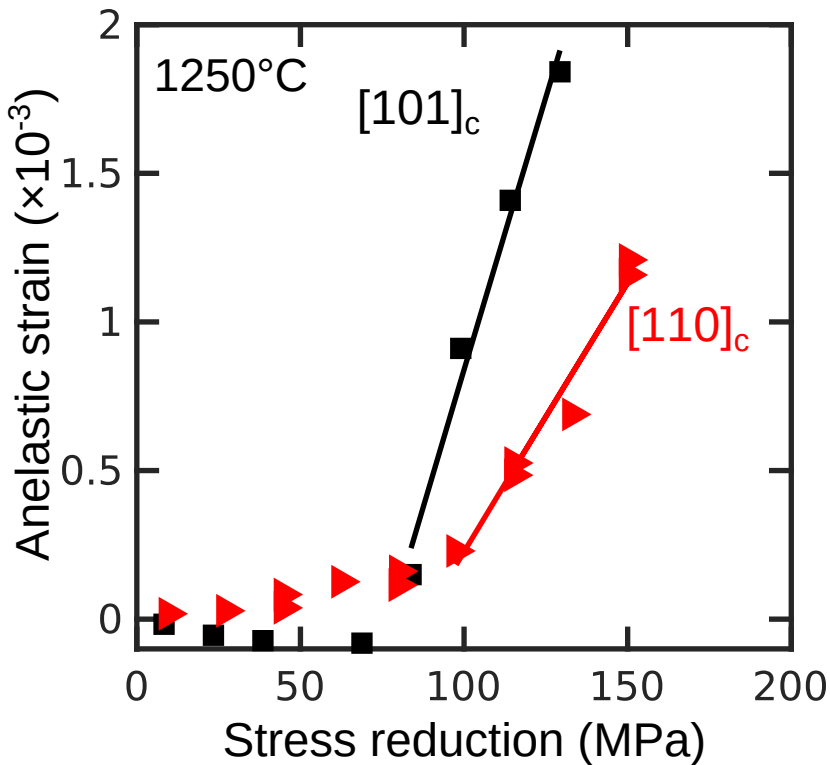


Figure 6.

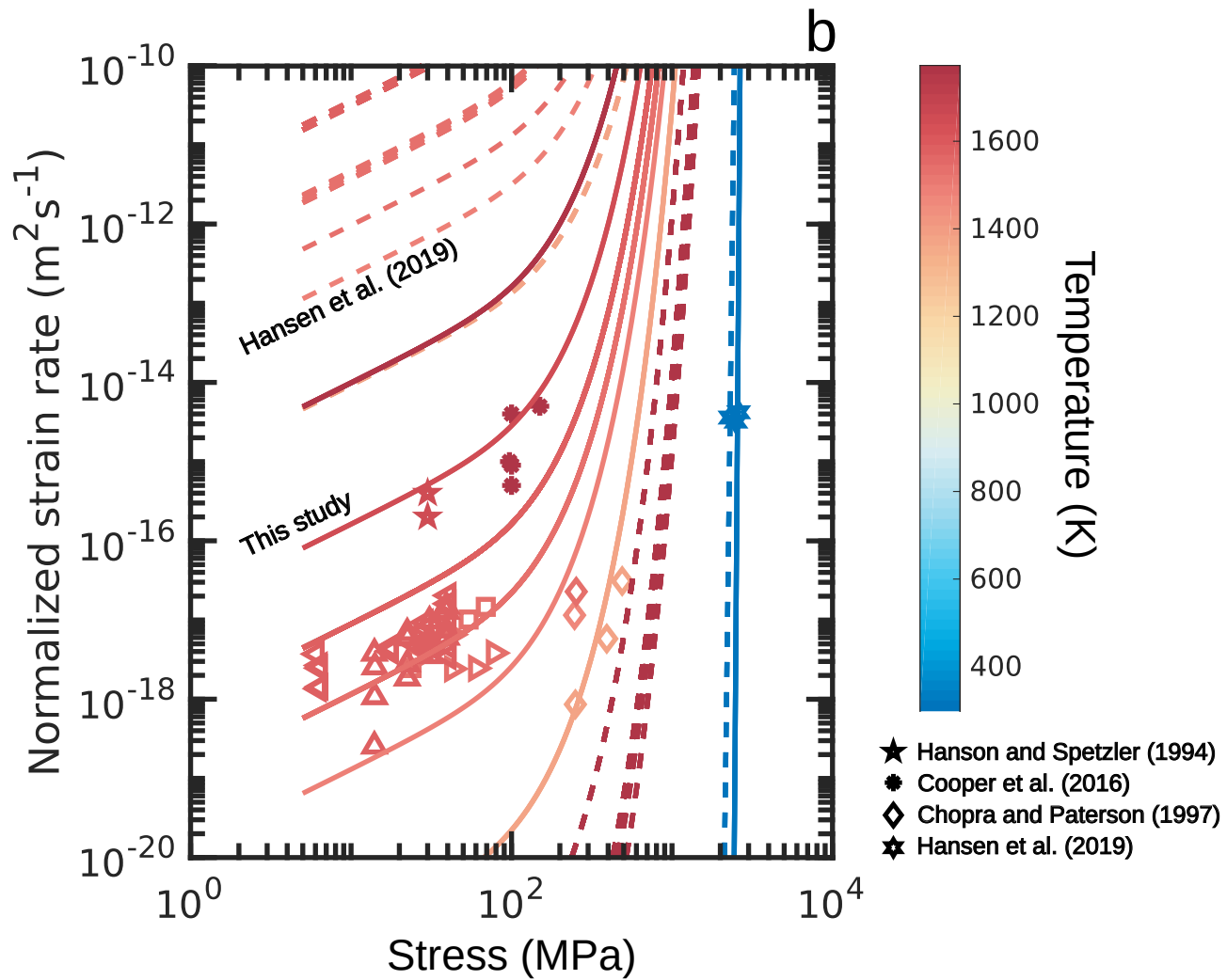
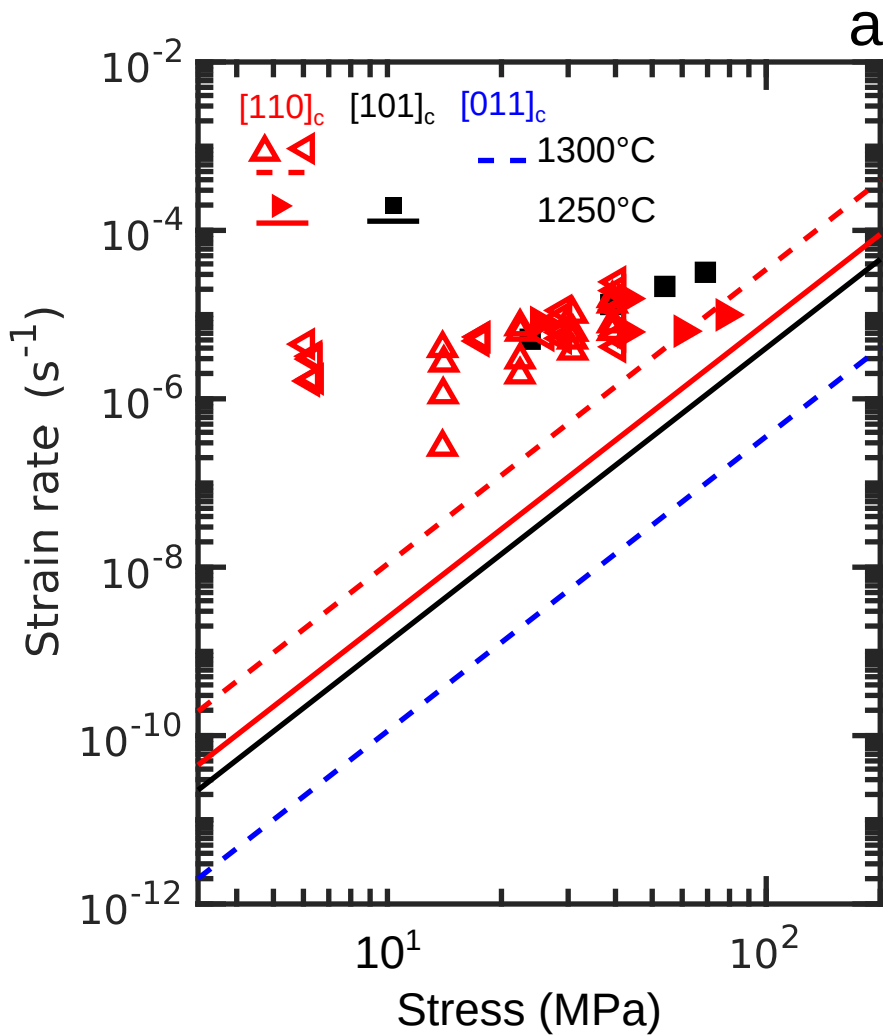


Figure 7.

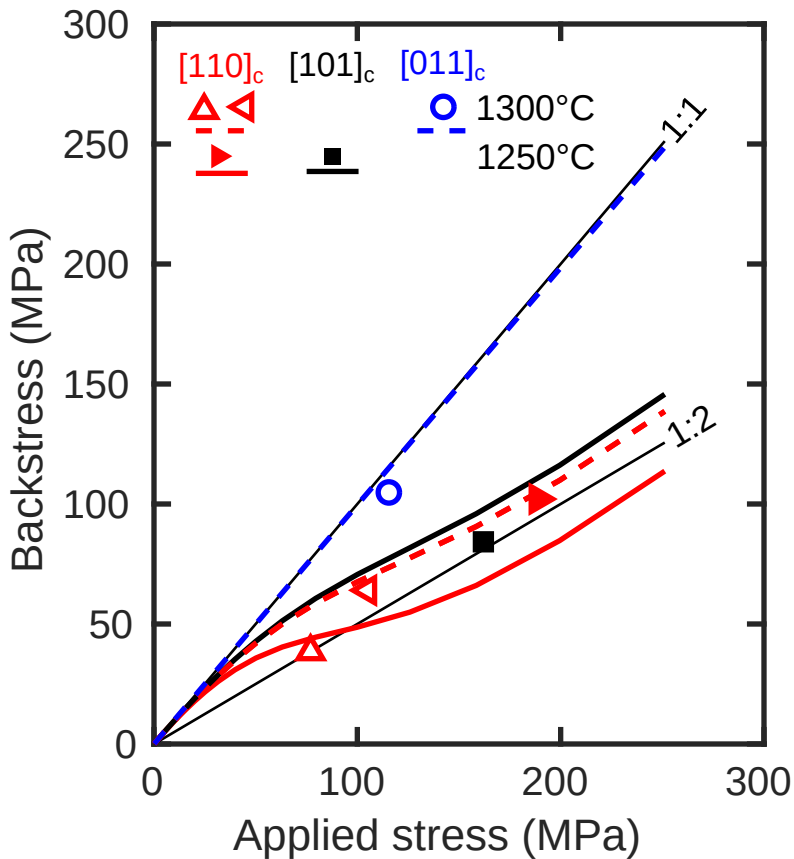
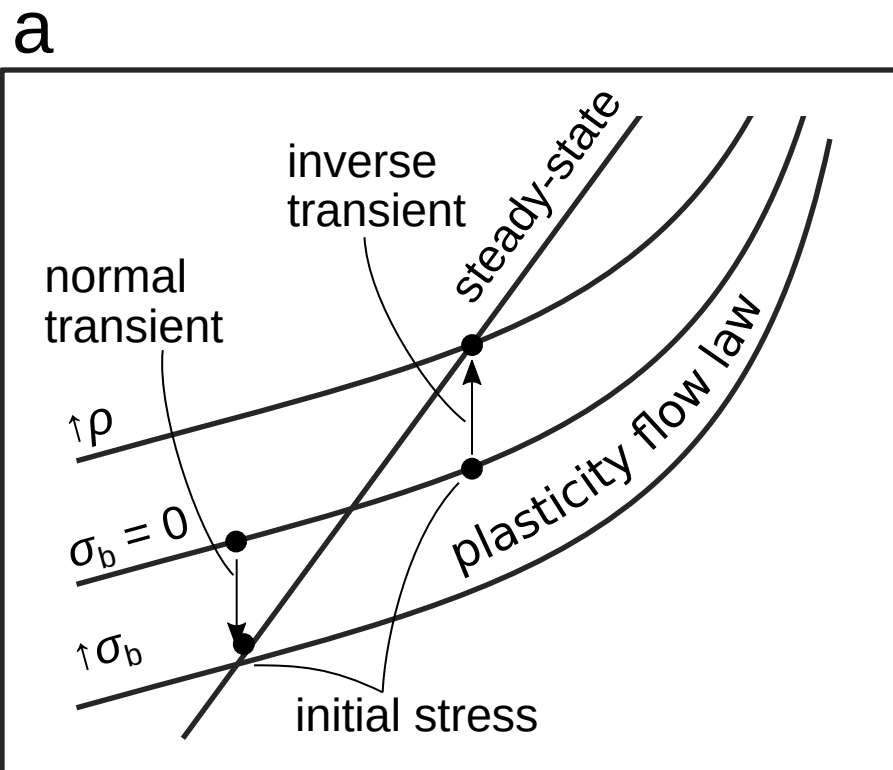
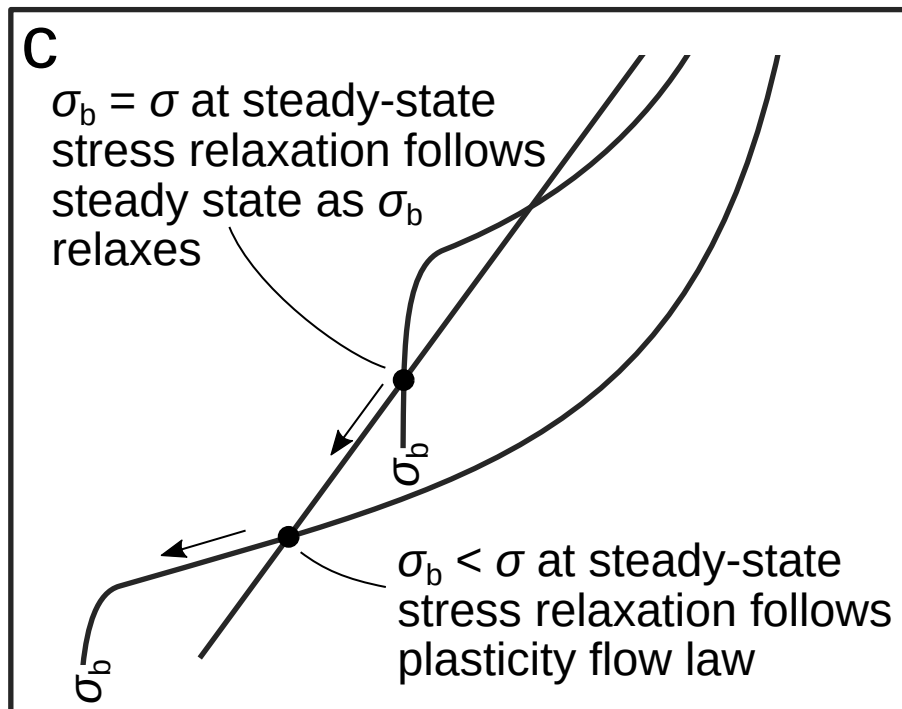


Figure 8.



log Strain Rate



log Stress

